DLK-dependent axonal mitochondrial fission drives degeneration following axotomy

Jorge Gómez-Deza [1], Matthew Nebiyou[1], Mor R. Alkaslasi[1], Francisco M. Nadal-Nicolás[2], Preethi Somasundaran[3], Anastasia L. Slavutsky[1], Michael E. Ward[4], Wei Li[2], Trent A. Watkins[3,5], Claire E. Le Pichon[1]

[1] *Eunice Kennedy Shriver* National Institute of Child Health and Human Development, National Institutes of Health, Bethesda, United States
[2] National Eye Institute, National Institutes of Health, Bethesda, United States
[3] Department of Neurosurgery, Baylor College of Medicine, Houston, TX.
[4] National Institute of Neurological Disorders and Stroke, National Institutes of Health, Bethesda, United States
[5] Department of Neurology, University of California at San Francisco

Abstract

Currently there are no effective treatments for an array of neurodegenerative disorders to a large part because cell-based models fail to recapitulate disease. Here we developed a reproducible human iPSC-based model where laser axotomy causes retrograde axon degeneration leading to neuronal cell death. Time-lapse confocal imaging revealed that damage triggers an apoptotic wave of mitochondrial fission proceeding from the site of injury to the soma. We demonstrated that this apoptotic wave is locally initiated in the axon by dual leucine zipper kinase (DLK). We found that mitochondrial fission and resultant cell death are entirely dependent on phosphorylation of dynamin related protein 1 (DRP1) downstream of DLK, revealing a new mechanism by which DLK can drive apoptosis. Importantly, we show that CRISPR mediated *Drp1* depletion protected mouse retinal ganglion neurons from degeneration after optic nerve crush. Our results provide a powerful platform for studying degeneration of human neurons, pinpoint key early events in damage related neural death and new focus for therapeutic intervention.

Introduction

Neuronal death and axon loss are universal hallmarks of neurodegeneration, relevant to Alzheimer's disease, ALS and other neurodegenerative diseases. However, our understanding of the mechanisms controlling axon degeneration and neuron death is incomplete. Advances in this area have enormous potential to benefit all types of neurodegenerative conditions including those arising from nerve injury and traumatic brain injury.

Separate mechanisms regulate axon degeneration and neuronal apoptosis [1]. For example, deletion of BAX (BCL-2-associated X protein), a central regulator of apoptosis, does not protect axons from Wallerian degeneration. On the other hand, BAX deletion protects neurons following trophic factor withdrawal, a developmental model of axon degeneration and death [2-4] . SARM1 is the central executioner of Wallerian axon degeneration [5, 6]. However, it is unclear how universal this pathway is for axon degeneration in the context of disease since some neurodegenerative models are not rescued by loss of SARM1 [7, 8]. Furthermore, while most neurodegenerative diseases involve loss of axons and cell bodies, Wallerian axon degeneration occurs independently from neuronal cell death.

Mitochondria are a central hub of axon health regulation, at the nexus of axonal energy production, oxidative stress, and calcium buffering [9, 10]. They also play critical roles in degeneration and regeneration [11, 12]. Healthy maintenance of the mitochondrial network is mediated by a balance of mitochondrial fission and fusion regulated by specialized machinery [13]. Interestingly, mutations in some of these genes cause neurodegenerative conditions such as motor and sensory neuropathy (eg. Mfn1 in Charcot-Marie-Tooth [14]). A key player in the mitochondrial fission process is dynamin related protein 1 or DRP1, a GTPase that oligomerizes around the outer mitochondrial membrane to cause mitochondrial fission [15]. DRP1 also regulates apoptosis [13, 16-18]. Under conditions that drive apoptosis, DRP1 promotes a type of apoptotic mitochondrial fission in which BAX permeabilizes the outer mitochondrial membrane, allowing the release of pro-apoptotic factors such as cytochrome c [19, 20].

Much of what we know about mechanisms regulating neuron degeneration and death comes from a wealth of studies of apoptosis in cell lines (but not neurons), or from animal models (neurons, but not human). How translatable this work is and how applicable to neurons remains to be determined. Recent advances in iPSC-derived neuron techniques now enable the generation of a diverse range of human neuron subtypes. These efforts have already generated exciting findings in the neurodegeneration field [21-23]. We therefore set out to study axon injury using a widely adopted glutamatergic neuron model produced by directed differentiation of human iPSCs (i3Neurons [24, 25]).

We and others have shown that the dual leucine zipper kinase (DLK, or MAP3K12), is a key regulator of axon degeneration and a driver of neuron cell death [26-30]. The canonical DLK pathway involves a phosphorylation cascade downstream of DLK homodimerization and a transcriptional stress response, including phosphorylation of the transcription factor cJun [30].

Despite its consideration as a drug target for several neurological conditions [31-33], relatively little is known about DLK function in human neurons.

Here, we investigate the behavior of i3Neurons following laser axotomy, and the role of DLK in the injury response of human neurons. Following axotomy, we observe progressive retrograde axon degeneration from the injury site back towards the cell body, causing subsequent neuronal death, and establishing a unique human model of neurodegeneration. This contrasts with the behavior of cultured mouse neurons, which survive and regenerate after this type of injury [34, 35], but resembles the pattern of neurodegeneration observed in optic nerve injuries in living mice [36] .

We find that in axons proximal to the injury, mitochondria shrink and undergo DRP1-dependent fission in a retrograde wave from the damage site, leading to apoptosis of the cell body. DLK regulates mitochondrial fission via phosphorylation of DRP1 at serine 616, defining a new substrate of the DLK signaling pathway. Such DRP1 phosphorylation is necessary for localization of BAX to axonal mitochondria, which causes axon degeneration. Blocking DLK or DRP1 protects axons from degeneration and neurons from cell death both in human i3Neurons *in vitro* and *in vivo* in the mouse. This study identifies a novel signaling mechanism for DLK that drives local axon degeneration without the need for transcription. Our findings reveal an apoptotic cascade that is initiated in the axon that both underlies a form of non-Wallerian axon degeneration and drives neuronal cell death.

Results

Axotomy in human neurons causes both proximal and distal axon degeneration

Axotomy has often been used as a method to study axon degeneration. After axotomy, the distal portion of the axon undergoes Wallerian degeneration, a phenomenon controlled by the NADase SARM1, the key executioner of this type of axon degeneration [5, 6]. To study the response of human neurons to axotomy, we performed laser axotomies in i3Neurons that were sparsely transduced with a fluorescent protein to visualize individual neurons (Fig. 1a). The distal portion of these axons underwent Wallerian degeneration as expected (Fig. 1b-c). To our surprise, we observed that the portion of the axon proximal to the injury and still connected to the cell body underwent progressive retrograde axon degeneration (Fig. 1b-c). Because SARM1-dependent degeneration relies on the loss of the axon survival factor NMNAT2, which occurs when the axon is severed from the cell body, we hypothesized that the proximal axon degeneration we observed might not rely on SARM1 and could provide an opportunity to elucidate novel pathways of axon degeneration.

We tested the requirement for SARM1 in the degeneration of axons both proximal and distal to the injury site. Using CRISPR/Cas9, we knocked out SARM1 in i3Neurons [37]. We then axotomized these neurons and control neurons and imaged the axon on both sides of the injury. As expected, SARM1 was necessary for distal, but not proximal, axon degeneration (Fig. 1b-c). We therefore investigated the mechanisms underlying proximal axon degeneration in these neurons. For the remainder of the study, we focus specifically on the axon segment proximal to the injury site.

Axotomy in human neurons triggers a wave of DRP1-dependent mitochondrial fission

Mitochondria play pivotal roles in axon degeneration, due to their importance in energy production, calcium homeostasis, production of reactive oxygen species and signaling [38, 39]. We transduced i3Neurons with a mitochondrial-targeted GFP and plated them in the center of wells to allow axons to project outwards and visualize individual axons. After axotomy, mitochondria underwent rapid shrinkage (Fig. 1d-g; Video S1) and increased in number (Fig. 1h). Using live imaging, we determined that the increase in mitochondrial number was due to fission events rather than mitochondrial transport and localization to the site of injury. Mitochondrial fission was most evident from close analysis of live imaging (Video S1 and Fig. 1d-e). This phenomenon was observed within 5 seconds after axon injury and was not affected by distance from the damage site from the cell body (Fig. S1a).

Mitochondrial fission is a dynamic process that is regulated by proteins localized in the inner and outer mitochondrial membranes [15]. A critical regulator of fission is dynamin related protein 1 (DRP1), a cytoplasmic GTPase. DRP1 is recruited to the outer mitochondrial membrane and helically oligomerizes around the mitochondrion to constrict it and bring about scission of the membrane. To test whether the fission we observed was dependent on DRP1, we knocked down DRP1 using CRISPR interference by expressing a previously validated guide RNA to DRP1 in i3Neurons expressing a catalytically dead Cas9 (dCAS9) [21, 37]. DRP1 knockdown prevented the

138 increase in mitochondrial particle number (Fig. 1h). We confirmed this result by inhibiting DRP1
139 using P110, a peptide that blocks the interaction between DRP1 and FIS1 (mitochondrial fission
140 protein 1), another protein that is essential for fission (Fig. 1i). In line with previous reports [40,
141 41], these events were dependent on calcium influx into the injured axon which, when buffered
142 using BAPTA-AM, also prevented mitochondrial fission (Fig. S1a-d; Videos S2-5).
143
144
145 **Mitochondrial fission precedes proximal axon degeneration**
146 To characterize the spatial and temporal dynamics of the axonal response to injury, we analyzed
147 mitochondrial fission and axon degeneration in 100 µm segments of the axon relative to the
148 injury site every 10 min following axotomy. This analysis revealed that mitochondrial fission
149 began seconds after injury and progressed in a retrograde manner back towards the cell body.
150 One hour after axotomy, mitochondria 500 µm away from the damage site had undergone fission
151 (Fig. 1j-k, Video S6). This fission preceded a slower retrograde wave of axon degeneration back
152 towards the cell body (Fig. 1l-m, Video S7).
153
154 Time lapse imaging of the cell bodies of axotomized neurons revealed that the retrograde wave
155 of axon degeneration was followed by fragmentation of mitochondria in the soma and cell death
156 (Fig. 1n-o; Videos S8-9). Axotomy led to death of 84% of cells analyzed. We have thus uncovered
157 an exciting new human neuron model in which axon injury initiates progressive retrograde axon
158 degeneration that ultimately results in neuronal cell death.
159
160
161 **DLK regulates axotomy-induced mitochondrial fission**
162 To understand mechanisms governing neurodegeneration in this model, we started by examining
163 a pathway involved in the cellular response to axon injury. The dual leucine zipper kinase (DLK;
164 MAP3K12) is a key regulator of the axon damage response and neuronal cell death [29, 42].
165 Because mitochondria are critical regulators of axon degeneration, we were curious whether DLK
166 protein might localize to axonal mitochondria. In i3Neurons, we observed association of
167 endogenous DLK with 77% of axonal mitochondria (Fig S2a-c). We further corroborated this
168 association by immuno-EM (Fig. S2d), and through observation of DLK co-trafficking with
169 mitochondria (Fig. S2e).
170
171 To investigate how DLK responds to axon damage in human neurons, we performed laser
172 axotomies and live imaging of GFP-tagged DLK and mitochondria. We observed an intriguing
173 presence of DLK puncta at 45% of sites of mitochondrial fission (Fig. 2a-b, Video S10). To
174 determine whether DLK influences mitochondrial fission, we generated DLK KO neurons using
175 CRISPR/Cas9 (Fig. S2f). The knockout neurons were validated for absence of DLK protein by
176 immunofluorescent staining and western blotting (Fig. S2g-h). In the undamaged condition, we
177 observed no mitochondrial phenotypes in these cells including number, size, movement, and
178 oxygen consumption rate (Fig. S2i-p). Strikingly, DLK KO neurons did not exhibit the axonal
179 mitochondrial fission we had observed in response to axotomy in wild type neurons (Fig. 2c-d;
180 Videos S11-12). Corroborating this result, pharmacological inhibition of DLK using GNE3511
181 prevented mitochondrial fission after injury (Fig. 2e, Videos S13-14).

182
183 To better understand the mechanism by which DLK regulates mitochondrial fission, DLK KO
184 neurons were transduced with wild type DLK or 2 mutant versions of DLK. DLK C127S cannot be
185 palmitoylated, hindering its ability to properly signal [43] . Kinase dead DLK (S302A) cannot be
186 trans-phosphorylated and is catalytically inactive [27, 44]. Only the expression of wild type DLK
187 rescued the fission phenotype in DLK KO neurons (Fig. 2f; Videos S15-17), indicating DLK kinase
188 activity is critical for this process.
189
190 We next tested whether inhibiting the c-Jun N-terminal kinases (JNK), known downstream
191 players of the DLK pathway, reduced mitochondrial fission after axotomy. Neurons exposed to
192 JNK inhibitor (JNKi) showed a significant reduction in mitochondrial fission following axon injury
193 (Fig. 2g-h). We thus uncover a role for DLK in initiating a wave of mitochondrial fission after injury.
194
195
196 **DLK kinase is necessary for DRP1 to induce mitochondrial fission**
197 DRP1 phosphorylation state regulates its function, with phosphorylation at serine 616 promoting
198 mitochondrial fission [45]. We speculated that DLK might be required for phosphorylation of
199 DRP1 at this residue. In order to more easily study this signaling mechanism, we turned to a
200 heterologous system, HEK293 cells, that do not express DLK. Overexpression of DLK in these cells
201 can be used to study DLK signaling since its homodimerization is sufficient to drive pathway
202 activity [44, 46].
203
204 Expression of wild type DLK, but not DLK C127S (palmitoyl-site mutant) or DLK S302A (kinase
205 dead), resulted in activation of DLK signaling as reflected by the increased phosphorylation of its
206 downstream target c-Jun (Fig. 3a-b). Interestingly, when we co-expressed DLK and DRP1,
207 phosphorylation at S616 was increased in this model of DLK activation (Fig. 3a,c), but not with
208 mutant DLK, showing that DLK activity is sufficient to cause DRP1 S616 phosphorylation. Levels
209 of total DRP1 remained unchanged, as did levels of S637 pDRP1, a site whose phosphorylation is
210 thought to impair DRP1 GTPase activity [47, 48] (Fig. 3a, d-e).
211
212 To further validate that DLK signaling causes DRP1 phosphorylation, we purified GST-DRP1 from
213 HEK293 cells expressing wild type DLK or DLK S302A, and performed targeted mass spectrometry
214 to quantify DRP1 phosphorylation. The relative abundance of phospho-DRP1 S616 peptides was
215 significantly increased only in the HEK293 cells expressing wild type but not kinase dead DLK (Fig.
216 3f). These results demonstrate that DLK kinase activity can promote DRP1 phosphorylation at
217 S616.
218
219 To further examine this phosphorylation event, we performed an *in vitro* kinase assay using
220 proteins separately purified from HEK293 cells. Incubation of DRP1 with wild type DLK increased
221 pDRP1 S616, whereas incubation with kinase dead DLK did not (Fig. S3a-c). We wondered
222 whether this DLK kinase activity on DRP1 was occurring via the canonical DLK kinase cascade,
223 since purification of DLK from HEK cells could result in isolation of the entire DLK signaling
224 complex including downstream kinases MAP2K and JNK. We detected JNK to be associated with

225 the DLK we pulled down, suggesting this was via canonical MAP3K signaling (Fig S3d). We also
226 found that DLK inhibitor and JNK inhibitor (but not p38 inhibitor) could block the phosphorylation
227 of DRP observed in the heterologous expression of DLK in HEK cells (Fig S3d-f). Together, these
228 data demonstrate that DRP1 is a novel substrate of DLK signaling that occurs via the canonical
229 DLK kinase cascade. To our knowledge, DRP1 is only the second substrate of DLK/JNK signaling
230 to be defined after cJun.
231
232 We analyzed mitochondrial morphology in the HEK293 cells to examine whether DRP1
233 phosphorylation caused by heterologous expression of DLK in HEK cells led to fission. Similar to
234 what we had observed in injured axons, DLK signaling resulted in an increase in mitochondrial
235 fragmentation (Fig. 3g-h). DLK-induced mitochondrial fragmentation was prevented by knocking
236 down DRP1 (Fig. 3i-k). These data identify DLK as a novel kinase upstream of DRP1 whose role is
237 to drive mitochondrial fission via phosphorylation of DRP1 at serine 616.
238
239
240 **Axotomy causes DLK-dependent phosphorylation of DRP1**
241 To validate these results in the i3Neurons, DLK KO or WT neurons were center-plated such that
242 axon fractions could be harvested to examine axonal DRP1 phosphorylation after injury (Fig. 4a).
243 Two hours after axotomy, phospho-DRP1 S616 (pDRP1 S616) was increased in axons but not cell
244 bodies of wild type neurons. However, as predicted, the increase in p-DRP1 did not occur in DLK
245 KO axons (Fig. 4b-e). The increase in pDRP1 S616 in wild type but not DLK KO axons was further
246 validated by immunostaining (Fig. 4f-g).
247
248 To examine whether DRP1 phosphorylation at S616 also occurs *in vivo*, we performed optic nerve
249 crush in mice. Increased pDRP1 S616 relative to total DRP1 was detected in optic nerve proximal
250 to the crush site 24 hours after injury (Fig. 4h-j). Levels of total DRP1 in injured nerves remained
251 unchanged (Fig. 4i,k).
252
253
254 **Inhibiting DRP1 delays axon degeneration and neuron death**
255 Since axotomy leads to progressive degeneration of the axon proximal to the injury and
256 eventually to cell death, we asked to what extent DLK and DRP1 control the degeneration of each
257 compartment. DLK has been shown to contribute to axon degeneration and to neuron death in
258 many contexts [26-30, 42]. We hypothesized that the DLK pathway would promote axon
259 degeneration in axotomized human neurons. Whereas wild type axons had degenerated as early
260 as 4 hours after injury, DLK KO axons were still present after 24 hours (Fig. 5a-c). Axons of neurons
261 treated with JNK inhibitor were similarly protected (Fig S4c-d). Interestingly, in neurons with
262 CRISPRi knockdown of DRP1, axons were also protected from degeneration (Fig. 5d-f).
263
264 To determine whether loss of DLK or DRP1 also protected neurons from death, we followed the
265 fate of cell bodies of axotomized neurons. In control neurons we observed cell death in about
266 70% of cells after axotomy whereas only 18% of DLK KO cells and 33% of DRP1 knockdown cells
267 died (Fig 5g-l). These results demonstrate that both DRP1 and DLK are key regulators of neuronal

268 cell death after axotomy. Interestingly, inhibiting transcription using actinomycin D (ActD)
269 protected neurons from cell death but did not prevent the retrograde axon degeneration (Fig
270 S4a-b), suggesting that DLK drives neuronal degeneration via distinct mechanisms depending on
271 the compartment.
272
273
274 **Loss of DRP1 prevents neuron death after axotomy *in vivo***
275 We then asked how universal this pathway is, or whether it was unique to the i3Neuron model.
276 It has been established that silencing DLK blocks retinal ganglion cell (RGC) death after optic nerve
277 crush [27, 28, 33, 36]. However, DRP1 has not previously been implicated downstream of this
278 DLK signaling. To knock down DRP1, we used an AAV delivery strategy to express a small Cas9
279 (sa-Cas9) together with a guide RNA to DRP1 [49] (Fig 6a). AAVs were injected into the intravitreal
280 space to transduce RGCs. Three weeks after the injection, DRP1 protein levels were significantly
281 reduced in the optic nerve of mice that had received gRNA DRP1 but not control scrambled gRNA,
282 validating this approach (Fig 6b-c).
283
284 Optic nerve crush was performed two weeks after AAV injection, and retinas were harvested 3
285 days post injury, a time point at which injured RGCs express cleaved caspase 3 (Fig. 6a). The
286 number of cleaved caspase 3-positive RGCs with saCas9 and a control gRNA was similar to a
287 control virus expressing just EGFP (55 ± 7.83 and 61 ± 6.24, respectively; average caspase-positive
288 cell count per ROI +/- SEM). However, knocking down DRP1 significantly reduced the caspase
289 positive cell count to 20 ± 8.93 (Fig. 6d-e), showing that apoptosis of RGCs relies on DRP1.
290
291 We performed a parallel experiment with the same viral strategy for DRP1 knockdown to assess
292 RGC survival 7 days after the injury. Using the RGC marker RBPMS, we found that DRP1
293 knockdown protected RGCs from axotomy-induced death (Fig 6f-h), increasing the total RGC
294 number per retina from $17{,}423 \pm 379$ to $22{,}273 \pm 789$ (average +/- SEM). Together, these
295 experiments demonstrate that DRP1 contributes to neuronal cell death after axon injury *in vivo*.
296
297
298 **BAX mediates axon degeneration and cell death after axotomy**
299 To better understand the type of axon degeneration and cell death observed in our study, we
300 asked whether they occurred via canonical pathways of apoptosis, and in particular whether they
301 involved BAX. In models of apoptosis, DRP1 contributes to BAX recruitment to mitochondria [50],
302 and DRP1 and BAX interact to drive mitochondrial depolarization and fragmentation [19, 51].
303 Jenner et al. showed a close interaction between DRP1 and BAX in HEK cells undergoing apoptosis
304 using a fluorescence complementation biosensor (ddRFP [52]). This system produces enhanced
305 red fluorescence upon dimerization of A_1 and B_1 proteins. Using A_1-DRP1 and B_1-BAX fusion
306 constructs, we tested whether DRP1 and BAX closely interact in the axon after injury. One hour
307 after axotomy, we observed a significant increase in red fluorescence. The interaction between
308 DRP1 and BAX occurred at mitochondria as shown by co-localization with mito-GFP (Fig. 7a).
309 However, DLK inhibitor GNE3511 reduced their interaction (Fig. 7a-b). To test whether the
310 interaction between DRP1 and BAX was dependent on DRP1 phosphorylation at S616, we
311 mutated the B_1-DRP construct to carry a S616A point mutation, preventing its phosphorylation

312 at this site. A_1-BAX and B_1-DRP1 S616A did not show the increase in red fluorescence,
313 demonstrating that the BAX-DRP1 interaction is more likely to occur if DRP1 is phosphorylated at
314 S616 (Fig. 7c), which requires DLK (Fig. 3).
315
316 We next tested whether inhibiting BAX would prevent cell death and axon degeneration in
317 i3Neurons using BAI, a highly selective small molecule inhibitor of BAX [53]. BAX inhibition
318 significantly preserved cell bodies of axotomized neurons (Fig. 7d-e). BAX inhibition also
319 significantly reduced axon degeneration measured 24 hours after injury (Fig. 7f), indicating that
320 BAX is a key mediator of axon degeneration and cell death after axotomy.
321
322 Finally, we asked whether local activation of BAX in the axon was sufficient to cause axons to
323 degenerate. Other studies have shown stimulation of BAX with a Bcl-x antagonist causes axon
324 degeneration [3, 54]. We grew i3Neurons in microfluidic chambers to physically isolate axons
325 from cell bodies and dendrites. BAX activator (BAX-A), which binds to the N-terminus of BAX to
326 promote its oligomerization [55], was added to the axon compartment, and we measured axon
327 integrity 24 hours later. We also performed this experiment in the presence of DLK inhibitor
328 GNE3511 (Fig. 7h). Local activation of BAX caused axons to degenerate, independently of DLK
329 inhibition (Fig. 7h-i), suggesting BAX signaling is downstream of DLK.
330
331 Together, our data reveal a local DLK signaling cascade within the axon that drives retrograde
332 axon degeneration after damage and does not require transcription. Starting at the site of
333 damage, the DLK/JNK complex locally phosphorylates DRP1, recruiting BAX to mitochondria and
334 producing an apoptotic cascade that spreads from the injury site back to the cell body where it
335 eventually results in cell death.

Discussion

In this work, we establish a novel and reproducible model of progressive axon degeneration and neuronal death in human neurons and unravel a cascade of events governing neurodegeneration after axon injury. We show that DLK kinase is required for DRP1 to drive mitochondrial fission and BAX-dependent apoptosis that originates in the axon and leads to degeneration of the axon followed by the cell body. We demonstrate the relevance of this pathway *in vivo*, extending from cultured human neurons to retinal ganglion cells of mice with optic nerve crush injuries. We hypothesize this pathway is broadly implicated in neuronal degeneration caused by axon damage, such as spinal cord injury and traumatic brain injury.

While BAX and DLK have separately been implicated in neuronal apoptosis of retinal ganglion cells after optic nerve crush [33, 36, 56, 57], an interaction between the two has not previously been reported, nor with DRP1. One study reported that DRP1-dependent mitochondrial fission occurs in axons after damage [58]. Here, we show how DLK, DRP1, and BAX cooperate to cause neuronal apoptosis after axon damage, and in particular, how the same apoptotic mechanism can follow axon loss [59] .

Until now, it was also unclear whether pathways distinct from SARM1 can mediate axon degeneration. Many clinical descriptions of axon degeneration refer to “dying back” as a pattern in which distal axons are lost before cell bodies [60, 61]. It has been suggested that dying back axon degeneration overlaps with Wallerian degeneration [62], but this remains unclear [63]. Although axon degeneration is rescued by SARM1 deletion in some models (e.g. chemotherapy-induced peripheral neuropathy [64]; TDP43-linked ALS [65]), it is not in others (SOD1 mouse model of ALS [7]; and optic nerve crush [8]). We have shown that a type of non-Wallerian axon degeneration that is more akin to apoptosis can occur after axon damage, and that it spreads retrogradely, similar to a dying back. It is possible that additional axon degeneration pathways also exist.

Therapeutically targeting this pathway offers multiple options. There is precedence for testing some of these strategies, such as blocking BAX [56, 57], or targeting mitochondrial dynamics [66], including promoting mitochondrial fusion [34] and blocking mitochondrial fission [67-70]. Blocking DLK signaling using small molecules has been considered [29, 32, 71], although a Phase I clinical trial in ALS patients was recently halted due to safety concerns [72]. However, specifically targeting the interaction between the DLK signaling complex and DRP1 has never been attempted.

In addition to protecting axons as we have shown, targeting DRP1 has the potential to protect dendrites [73]. However, it also has possible toxicity issues as mitochondrial fission is critical for regeneration and motor neuron survival after sciatic nerve injury [74]. A more complete understanding of DRP1 regulation in homeostatic and injury conditions will be helpful. For example, future studies may identify other targetable DRP1 phosphorylation sites in addition to serine 616 as well as additional kinases. To date, kinases of DRP1 that have been identified include CDK5 [75, 76], TBK1 [77], ERK1/2 [78, 79], CAMKIa [80] and CAMK2 [81]; here, we highlight DLK/JNK as a novel regulatory kinase upstream of DRP1 [82].

380
381 As a cytoplasmic facing kinase complex, DLK/JNK has the potential to regulate many substrates
382 of which we now identify DRP1. Additional substrates of the pathway will be of great interest to
383 uncover, as DLK is reported to associate with the plasma membrane, Rab3, Rab6, Rab7, Rab11,
384 Golgi-derived, and LAMP1-positive vesicles [43, 83]. Localization of DLK to mitochondria has also
385 recently been described in cultured mouse embryonic DRG neurons [83], corroborating our
386 observation of DLK-mitochondrial association.
387
388 Our study highlights a novel signaling pathway downstream of DLK. It has generally been thought
389 that DLK-dependent transcriptional events govern neuronal degeneration [36], but here we find
390 that transcription is dispensable for retrograde axon degeneration driven by DLK via DRP1. It will
391 be of interest to examine how the retrograde axon degeneration mechanism regulated by DLK-
392 DRP1 is coordinated with transcriptional regulation of cell death factors by DLK, for example BID
393 and PUMA [3].
394
395 DRP1-dependent apoptosis has been described in many cell types [17] however, its regulation by
396 DLK was not previously recognized. That axonal DLK can locally trigger this cellular apoptotic
397 pathway from a site of axonal injury that then spreads retrogradely to the cell body is distinct
398 from the previously recognized transcriptional regulation of apoptosis by DLK. Our results call to
399 mind new questions, such as how is DLK localized to the site of mitochondrial fission so it can
400 regulate DRP1 phosphorylation? Does it associate with factors like MFF, which is an essential
401 factor in recruiting DRP1 to mitochondria [84]? And what is the mechanism of activation of DLK
402 that would link it to mitochondrial fission? In the future, it will be of great interest to explore
403 under which conditions this pathway is activated, as well as the specificity of this pathway to
404 different neuronal subtypes.

405 **Methods**
406
407 **I3Neuron differentiation**
408 I3Neurons were differentiated as previously described. Briefly, i^3 iPSCs were dissociated using
409 Accutase (Life Technologies, A1110501). Cells were plated in Matrigel-coated (1:100 Corning)
410 plates in Neuronal induction media on day 0 (Knockout Dulbecco's modified Eagle's medium
411 (DMEM)/F12 medium; Life Technologies Corporation, 12660012), 1X N2 supplement (Life
412 Technologies, 17502048), 1× GlutaMAX (Thermofisher Scientific, 35050061), 1× MEM
413 nonessential amino acids (NEAA) (Thermofisher Scientific, 11140050), 10 µM ROCK inhibitor (Y-
414 27632; Tocris, 1254), and 2 µg/ml doxycycline (Clontech, 631311). Neuronal induction media was
415 changed once a day for 2 more days. On day 3 of induction, cells were dissociated using Accutase
416 and plated in dishes coated with poly-L-ornithine (PLO; 0.1 mg/ml; Sigma, P3655-10MG). Cells
417 were plated in neuronal maturation media (BrainPhys medium (STEMCELL Technologies, 05790),
418 1× B27 Plus Supplement (ThermoFisher Scientific, A3582801), 10 ng/ml BDNF (PeproTech, 450-
419 02), 10 ng/ml NT-3 (PeproTech, 450-03), 1 mg/ml mouse laminin (Invitrogen, 23017015), and 2
420 µg/ml doxycycline). Half of the neuronal maturation media was removed and replenished with
421 fresh media every 2-3 days.
422
423 **Lentivirus generation**
424 Lentivirus were generated as previously described [37], 7 million Lenti-X HEK-293T cells (Takara
425 Bio, 632180) were seeded in 9 mL DMEM. The next day, a transfection mix was prepared
426 containing 1 µg of Lenti plasmid, 3 µg of third generation packaging mix (1:1:1 mix of three
427 plasmids), 12 µL Lipofectamine 3000 Reagent (ThermoFisher, L3000008), and 250 µL Opti-MEM
428 I Reduced Serum Medium (GIBCO, 31985070). The mix was vortexed, spun down briefly,
429 incubated at room temperature for 40 minutes, then added dropwise to the HEK cells and gently
430 swirled to mix. The next day, the media was replaced with 18 ml fresh 10% FBS DMEM
431 supplemented with 1:500 ViralBoost (Alstem, VB100). Two days later, the media was collected
432 into a 50 ml Falcon tube, supplemented with 6 ml Lenti-X Concentrator (Takara Bio; 631231),
433 mixed thoroughly, and stored at 4°C for 48 hours. The supernatant was then spun down at 4°C
434 for 45 minutes at 1,500 x g. The supernatant was aspirated, and the pellet was resuspended in
435 500 µL of PBS.
436
437 **Plasmids and cloning**
438 All DLK (Ensembl CCDS: 55831) constructs and mutants were generated by Epoch Live Science
439 (Texas, USA) and cloned into a lentivirus-expressing backbone under a doxycycline-dependent
440 promoter. DLK was C-terminally tagged by inserting a glycine rich linker (3x GGGGS) followed by
441 EGFP, just before the stop codon. EYFP-DRP1 was obtained from Addgene (45160). For GST-
442 purification, DLK and DRP1 were N-terminally tagged into a GST-containing backbone using In-
443 fusion cloning (Takara Bio. 638945). Cyto-mAPPLE plasmid was a gift from Michael E. Ward
444 (NINDS). A_1-BAX and B_1-DRP1 were gifted by Dr. Ana J. Garcia-Saez (Max Plank Institute of
445 Biophysics). Mito-EGFP and Mito-RFP plasmids were gifts from Dr. Zu-Hang Sheng (NINDS).
446
447 **DRP1 knockdown using dead Cas9**

448 For DRP1 knockdown, we used CRISPRi-i[3] iPSCs containing a CAG promoter-driven dCas9-BFP-
449 KRAB cassette inserted into the CLYBL safe harbor locus (Addgene #127968). iPSCs were
450 transduced with control gRNA or a previously validated gRNA targeting DRP1[84] and differentiated
451 as described above.
452
453 **Laser Axotomies**
454 Laser axotomies were performed on 10-14 day old neurons using a Zeiss LSM 880 Upright 2-
455 Photon microscope equipped with an ablate laser. Temperature and CO_2 levels were maintained
456 using a Pecon microscope incubator. Ablation laser was set to 800 nm, 100% power and 100
457 iterations. Neurons were cultured in µ-Dish 35 mm dishes (Ibidi, 81156 or 81166 depending on
458 the application) in Hybernate E (Gibco A1247601), 1× B27 Plus Supplement (ThermoFisher
459 Scientific A3582801), 10 ng/ml BDNF (PeproTech 450-02), 10 ng/ml NT-3 (PeproTech 450-03), 1
460 mg/ml mouse laminin (Invitrogen 23017015), and 2 µg/ml doxycycline.
461
462 **Mitochondrial fission after axotomy**
463 iPSCs were differentiated as described above. On day 1 of differentiation, cells were transduced
464 with the appropriate lentivirus. Neuronal induction media was changed 24 hours later. On day 3
465 of differentiation, 50,000 cells were plated in a 5 µL drop of neuronal maturation media in the
466 middle of a 35mm dish (ibidi, 81156) for the axons to grow out from the center. Dishes were
467 incubated for 20 minutes at 37°C to allow cells to attach, and 2mL of neuronal maturation media
468 was then added to each well. Cells were fed with half-media changes every two days until the
469 day of the experiment. Laser axotomies were performed as described above. Single axons were
470 randomly selected. Five images were taken before axotomy every 5 seconds and axons were
471 imaged for 5 minutes after axotomy every 5 seconds. The number of mitochondrial particles was
472 quantified using imageJ imaging software and normalized to the number of mitochondria pre-
473 axotomy. When treating neurons with different chemical compounds, neurons were pretreated
474 for one hour prior to performing axotomies. The following compounds were used GNE3511 (500
475 nM, Sigma, 5331680001), JNKi (SP600125 1µM, Selleckchem S1460), P110 (1 µM, Tocris, 6897),
476 BAPTA-AM (10mM Tocris 2787), BSTA1 (BAX activator, 10 µM, Sigma SML2243) and BAI1 (BAX
477 inhibitor, 10 µM, Medchemexpress HY-103269).
478
479 **Axon separation and axotomies**
480 For axon separation experiments after axotomy, 1.5 million cells were plated in 150 µl of
481 maturation media in a strip in the center of a 6 cm dish. Cells were allowed to attach for 15
482 minutes at 37°C, after which 8 ml of media was added to the dish. Neurons were cultured for 1
483 month to allow for the axons to project outwards. Axotomy was performed using a sharp blade.
484 Axons and cell bodies were separated and processed for western blotting.
485
486 **Immunostaining of cells**
487 Cells were fixed in cold 4% PFA for 5-10 minutes, permeabilized using 0.1% TritonX in PBS for 5
488 mins and blocked in 5% normal donkey serum (NDS) in PBS at room temperature for 1 hour. Cells
489 were immunostained with the selected primary antibody in 2.5% NDS overnight at 4°C. Cells were
490 washed three times with PBS and stained with the appropriate secondary antibody at a
491 concentration of 1:500 in 2.5% NDS for 1 hour at room temperature. Cells were washed three

492 times with PBS and DAPI was used as a nuclear counterstain. Antibodies used against: βIII tubulin
493 (Thermo Fischer, 2G10, 1:500), pDRP1 S637 (CST, 4867S, 1:1000), DLK (DLK antibody developed
494 and kindly provided by Cell Signaling Technology, clone GF-23-1, 1:500), TOM20 (Santa Cruz,
495 SC-17764, 1:500).
496
497 **Calcium imaging**
498 Neurons were plated as described above in the center of a 35mm dish, and their axons were
499 allowed to grow outwards. 10-14 days post induction, neurons were treated with Fluo-4 AM cell
500 permeable calcium dye (ThermoFischer, F14201) following the manufacturers indications.
501 Axotomies were performed on single axons as described above and imaged every 2 seconds for
502 2 minutes after axotomy. Fluorescence intensities were calculated using ImageJ software and
503 normalized to pre-axotomy levels.
504
505 **HEK cell culture and transfection**
506 HEK-293T cells were cultured in DMEM (Gibco, cat. no 11995065) supplemented with 10% FBS
507 (Gibco; 10437028). For transfection, cells were dissociated using Trypsin-EDTA (0.25%)
508 (ThermoFischer, 25200056) and plated in DMEM, 10%FBS. The day after plating cells were
509 transfected with 1 µg DNA plasmid, 8 µl lipofectamine 2000 (Invitrogen, 11668030) for 24 hours.
510 For western blotting, cells were harvested in ice cold RIPA buffer (Invitrogen, 89901)
511 supplemented with protease inhibitors (Sigma, 11836153001) and PhosStop (Sigma
512 4906845001). For immunostaining, cells were fixed in 4% PFA for 10 minutes.
513
514 **Western blotting**
515 Protein concentrations were calculated using a BCA assay (ThermoFisher 23225). 10-20 µg of
516 total protein lysate was loaded into a 4–20% Mini-PROTEAN® TGX™ Precast Protein Gels (Biorad
517 4561095). Gels were transferred into PVDF membranes and blocked for 1 hour at room
518 temperature in 5% BSA. Membranes were incubated with the appropriate primary antibody in
519 2.5% BSA solution in a cold room, rocking, overnight. Membranes were washed 3 times with PBS
520 0.1% Tween solution. Secondary antibody was incubated for 1 hour at room temperature at a
521 concentration of 1:8000 in 2.5% BSA solution. Membranes were washed 3 times with PBS 0.1%
522 Tween solution prior to developing. Western blots were developed using Clarity Western ECL
523 Substrate (Biorad 1705061) and imaged using a ChemiDoc MP Imaging system (Biorad). Band
524 intensity was quantified using FIJI imaging analysis software. The following antibodies were used
525 at the concentrations stated: anti-DRP1 (Santa Cruz Biotechnology, sc-101270, 1:1000), anti-
526 pDRP1 S616 (CST 3455S, 1:1000), anti-ß Actin (Sigma A1978, 1:5000), anti-p-cJun S63 (CST 9261,
527 1:1000), anti-pDRP1 S637 (CST 4867S, 1:1000).
528 Abundance of phospho-DRP1/ total DRP1 was obtained running two western blots loaded with
529 the same amount of total protein. Phosphorylated and unphosphorylated DRP1 protein bands
530 were each normalized to actin levels, then the value for pDRP1 was divided by the value for DRP1
531 to obtain the relative levels of phosphorylated protein.
532
533 **Axon Degeneration index and neuron survival**
534 Induction of iPSCs into neurons was performed as described above. On day 1 of differentiation,
535 neurons were transduced with a cytoplasmic mApple (cyto mApple)-expressing lentivirus, and

536 the media was changed 24 hours later. On day 3 of differentiation, transduced neurons were
537 mixed with mixed with untransduced neurons at a ratio of 1:8000 to achieve sparse labelling of
538 neurons, and re-plated on a 35mm gridded dish (Ibidi 81166). On day 14 of differentiation, the
539 positions of selected axons or neuron somas was recorded and laser axotomies were performed
540 as described above. Dished were stored in a temperature and CO_2 controlled incubator until
541 imaged next. Injured axons and somas were re-located at different time points after axotomy
542 using the gridded dish and imaged. Axons were injured <1mm away from the soma. The axon
543 degeneration index was calculated as previously described [37]. The following compounds were
544 used: JNKi (SP600125 1µM, Selleckchem S1460), Actinomycin D (ActD) (Selleckchem S8964;
545 3µM).
546
547 **Airyscan imaging**
548 Neurons were plated in 1mm German Glass Coverslips thickness #1.5 (Electron Microscopy
549 Sciences 72290-04). 10-day old neurons were fixed with 4% PFA for 10 minutes at room
550 temperature. Cells were permeabilized with 0.1% Triton-X for 5 minutes and blocked in 5%
551 normal donkey serum (NDS) at room temperature for an hour. Primary antibody incubation was
552 carried out in 2.5% NDS overnight at 4°C. Cells were washed three times with PBS and stained
553 with the appropriate secondary antibody at a concentration of 1:500 in 2.5% NDS for 1 hour at
554 room temperature. Cells were washed three times with PBS and DAPI was used as a nuclear
555 counterstain. Coverslips were mounted using ProLong Glass antifade (Invitrogen P36980).
556
557 **Seahorse analysis**
558 For Seahorse analysis, 50,000 cells per well were plated after 3 days of induction in a specialized
559 Seahorse analyzer 96-well plate (Agilent, 103774-100). Cells were washed in PBS once and
560 incubated in a hypoxic chamber following the manufacturer's procedure. Seahorse analysis was
561 performed using a Seahorse XFe 96 Analyzer (Agilent). The average value for three wells was used
562 for analysis.
563
564 **Protein purification and *in vitro* kinase assay**
565 DLK and DRP1 were cloned into a pcDNA3-C-terminal GST vector. 12 million HEK293 cells were
566 plated in 10 cm dished coated with Matrigel. The day after, cells were transfected with 10 µg
567 plasmids and 40 µl lipofectamine. 24 hours post transfection, cells were washed twice with PBS
568 and harvested in 880 µl ice cold RIPA buffer (Invitrogen, 89901) supplemented with protease
569 inhibitors (Sigma, 11836153001) and PhosStop (Sigma 4906845001). Lysates were sonicated and
570 spun at 18000 g 10 minutes at 4°C and the pellet was discarded. 500 µl Glutathione-Sepharose
571 beads (Sigma GE17-0756-01) were washed twice in 1ml in lysis buffer. Washed beads to 1 ml
572 lysate and incubate end-over-end shaking in cold room overnight. The next morning. Beads were
573 washed 4 times with lysis buffer + 0.4M NaCl. The protein-containing beads were pelleted by
574 spinning 1min 8000 rpm at 4°C, the supernatant was discarded, and the beads were resuspended
575 in fresh 200 mM glutathione 1X PBS solution for elution of the desired protein. The beds were
576 incubated for 20 minutes at room temperature shaking. The eluted protein and the beads were
577 separated by briefly spinning in a SpinX column tubes (Sigma CLS8162-24EA). The purity of
578 purified protein was by running 5 µg of protein on an SDS PAGE gel and performing Comassie
579 stain. The purified protein was stored at -80°C. For *in vitro* kinase assay, purified GST-DLK or GST-

580 DLK-S302A was mixed with purified GST-DRP1 at a 1:1 ratio in 50 µl kinase buffer (50mM TrisHCL
581 pH 7.5, 150mM NaCl, 10mM MgCl, 10mM $MnCl_2$, 1.8mM ATP) incubated for 60 mins at 37°C. In
582 vitro kinase assay was also performed in the presence of DLKi inhibitor GNE3511 (500 nM, Sigma,
583 5331680001) and JNKi (SP600125 1µM, Selleckchem, S1460). The reaction was terminated by
584 adding SDS gel loading buffer and the sample was subjected to western blotting.
585
586 **Phospho-mass spectrometry**
587 DRP1 bands, with ~0.5 µg protein on each band, were cut from SDS-PAGE. In-gel samples were
588 reduced with 10 mM Tris(2-carboxyethyl)phosphine hydrochloride, alkylated with N-
589 Ethylmaleimide, and digested with trypsin at 37°C for 18 hours. Peptides were extracted,
590 desalted and injected into a nano-LC-MS/MS system where an Ultimate 3000 HPLC was coupled
591 to an Orbitrap Lumos mass spectrometer (Thermo Scientific) via an Easy-Spray ion source
592 (Thermo Scientific). Peptides were separated on an ES902 Easy-Spray column (75-µm inner
593 diameter, 25 cm length, 3 µm C18 beads; Thermo Scientific) with mobile phase B (0.1% formic
594 acid in LC-MS grade acetonitrile) increased from 3% to 24% in 60 min. The flow rate was
595 maintained at 300 nl/min. MS and MS/MS data were acquired on Thermo Scientific Orbitrap
596 Lumos mass spectrometer. MS1 scans were acquired in orbitrap at of a resolution 120k with a
597 mass range of m/z 400-1500. MS2 scans were acquired in ion trap with ETciD method at normal
598 scan rate. The isolation width was 1.6 m/z. Ions were excluded after 1 acquisition and the
599 exclusion duration is 9 sec. MS1 scans were performed every 3 sec. As many MS2 scans were
600 acquired within each MS1 scan cycle. Proteome Discoverer software version 2.4 was used for
601 protein identification and quantification. Database search was performed against Sprot Human
602 database using Mascot search engine. Mass tolerances for MS1 and MS2 scans were set to 5 ppm
603 and 0.4 Da, respectively. Up to 2 missed cleavage was allowed for trypsin digestion. NEM on
604 cysteines was set as fixed modification. Oxidation (M) and Phosphorylation (STY) were searched
605 as variable modifications. Spectra of phosphopeptides matched by database search were
606 manually checked. The search results were filtered by a false discovery rate of 1% at the protein
607 level. Proteins detected with 1-2 peptides were further filtered out. Protein abundance values
608 were calculated by summing the abundance of unique and razor peptides matched to that
609 protein. Each sample group contains 4 replicates. The ratios were calculated using protein
610 abundance without normalization.
611
612 **Electron microscopy**
613 Neurons were plated in 1mm German Glass Coverslips thickness #1.5 (Electron Microscopy
614 Sciences, 72290-04). 10 Day old neurons were fixed with in 4% PFA, 1% Glutaraldehyde for 40
615 minutes. Fixed cells were placed in phosphate buffer containing 0.1% sodium borohydride to
616 inactivate residual aldehyde groups. Cells were then washed with phosphate buffer several times
617 until the solution was clear of bubbles. To improve reagent penetration, the cells were then
618 treated with phosphate buffer containing 0.05% Triton X-100. To prevent nonspecific binding of
619 the immunoreagents, cells were incubated in Aurion blocking solution for Goat gold conjugates
620 (Electron Microscopy Sciences, Hatfield, PA., containing phosphate buffer, pH 7.4, normal goat
621 serum (NGS), bovine serum albumin (BSA), and cold water fish skin gelatin (CWFG)). After
622 blocking, cells were incubated in the primary antibody, DLK (custom antibody from Cell Signaling
623 Technology, clone GF-32-1, 1:100) diluted with incubation buffer (phosphate buffer containing

624 0.2% Aurion acetylated bovine serum albumin (BSA-c), Electron Microscopy Sciences, Hatfield,
625 PA., 5% CWFG and 5% NGS, pH 7.4) for two hours at room temperature. After washes with
626 incubation buffer, cells were incubated in the secondary antibody Aurion ultra-small gold-
627 conjugated $F(ab')_2$ fragments of Goat anti-Rabbit IgG, (Electron Microscopy Sciences, Hatfield,
628 PA.) diluted 1:100 with incubation buffer overnight at 4°C. To remove unbound secondary
629 antibody, cells were washed thoroughly with incubation buffer and then with PBS. After washes,
630 cells were prepared for silver enhancement.
631
632 **Silver Enhancement and Cell processing for Electron Microscopy**
633 Cells were washed with MilliQ water and then transferred to Aurion R-Gent SE-EM silver
634 enhancement solution, Electron Microscopy Sciences, Hatfield, PA. and incubated at room
635 temperature for 35 minutes. The enhancement was stopped by washing cells several times in
636 MilliQ water. The following processing steps were carried out using the variable wattage Pelco
637 BioWave Pro microwave oven (Ted Pella, Inc., Redding, CA.): cells were rinsed in MilliQ water,
638 post-fixed in 1% osmium tetroxide made in MilliQ water, ethanol dehydration series up to 100%
639 ethanol, followed by a Embed-812 resin (Electron Microscopy Sciences, Hatfield, PA.) infiltration
640 series up to 100% resin. The epoxy resin was polymerized for 20 hours in an oven set at 60°C.
641 Ultra-thin sections (90nm) were prepared on a Leica EM UC7 ultramicrotome. Ultra-thin sections
642 were picked up and placed on 200-mesh cooper grids (Electron Microscopy Sciences, Hatfield,
643 PA) and post-stained with uranyl acetate and lead citrate. Imaging was performed on a JEOL-1400
644 Transmission Electron Microscope operating at 80kV and images were acquired on an AMT
645 BioSprint 29 camera.
646
647 **Generation of DLK KO iPSCs**
648 WT iPSCs were transfected with Cas9-GFP, and two gRNA containing plasmids targeting exons 3
649 and 5. gRNA expressing plasmids were purchased from Sigma Aldrich (U6-gRNA:hPGK-puro-2A-
650 tBFP, gRNA1: CCCAGGCTCCCTGCTACTGCAT, gRNA 2: TCCTTTGGCGTGGTGCTATGGG). 1 day after
651 transfection, expression of Cas9 and gRNAs was validated by the expression of GFP and BFP
652 respectively and iPSCs were treated for 3 days with 10 µM Puromycin (Invitrogen A11113803)
653 and allowed to recover for 3 days. Cells were then dissociated with accutase for 10 minutes and
654 dissociated my pipetting forcefully 10 times. A 1:2 serial dilution was then performed in two 6
655 well plates. iPSCs were fed every 3 days until individual colonies were figure visible (usually 10-
656 14 days). Individually colonies were picked using a P1000 pipette and transferred into individual
657 wells in a 24-well plate. Individual clones were allowed to expand, passaged and their DNA was
658 extracted for DLK KO validation using PCR (Forward primer: TCAGGTGAATGCTGAGCCAGCT,
659 reverse primer: TGGAGACTGTTGCTTCCCACAC). A shorter band from ~1200bp to ~200bp was
660 expected if the KO was successful. Potential clones were sequenced. Further validation was
661 performed by differentiating potential clones into neurons and knock out of DLK was validated
662 by western blotting and immunofluorescence.
663
664 **Animals**
665 All animal care and experimental procedures were performed in accordance with animal study
666 proposals approved by the National Institute of Child Health and Human Disease Animal Care and
667 Use Committee (animal protocol number 20-003, Le Pichon lab), National Eye Institute (animal

668 protocol number NEI-606, Li lab) and by the Baylor College of Medicine ACUC (animal protocol
669 #AN-7208; Watkins lab). C57Bl/6J (Jax#000664) mice of both sexes, aged between 6-10 weeks
670 old, were used in this study.
671
672 **Mouse optic nerve preparation for Western blotting**
673 Mice were anesthetized with 2.5% avertin followed by decapitation. Each eye was carefully
674 removed from orbit with the optic nerve attached. The proximal segment of the injured nerve
675 was harvested and dissected on a cold (4°C) surface in PBS containing protease inhibitors (Sigma
676 11836153001) and PhosStop (Sigma 4906845001). Nerves from 4-6 mice were pooled to obtain
677 enough protein for each lane of a Western blot. Nerves were mechanically lysed in 40 µl ice cold
678 RIPA buffer (Invitrogen 89901) supplemented with protease inhibitors (Sigma 11836153001) and
679 PhosStop (Sigma 4906845001) for 2 minutes using a micro pestle. Nerves were then sonicated
680 for 15 minutes at 4°C. Protein lysates were centrifuged at 18 000g, 4°C for 10 minutes and the
681 pellet was discarded. The samples were subjected to the western blotting procedure described
682 above.
683
684 **Adeno-associated virus (AAV)**
685 Adeno-associated viral vectors carrying human synapsin-1 (*hSyn1*) promoter driving expression
686 of saCas9-U6-control, saCas9-U6-DRP1-gRNA, or eGFP were generated by Epoch Life Sciences Inc.
687 The plasmids were then packaged into AAV2 capsids at the Optogenetics and Viral Vector Core
688 at Duncan Neurological Research Institute, Houston.
689
690 **Intravitreal injections**
691 Mice to be injected were anesthetized with 3% isoflurane. The eyes were sterilized by 3 repeated
692 applications of 5% ophthalmic betadine (Henry Schein #6900250), Opti-clear ophthalmic eye
693 wash (Akorn #NDC 17478-620-04) and a dry wipe. A topical anesthetic 0.5% proparacaine HCl
694 ophthalmic solution (Henry Schein #1365345) was applied. The eyeball was punctured using a 5-
695 µl Hamilton syringe loaded with a custom 33-gauge needle (Hamilton #7803-5) and some of the
696 intraocular pressure was relieved. The same puncture site was used to reinsert the Hamilton
697 needle and 2 µl of AAV in titers ranging from 10^{12} -10^{13} vg/ml was delivered per eye.
698
699 **Intra-orbital optic nerve crush (ONC)**
700 Two weeks after intravitreal injections, animals underwent optic nerve crush surgeries. Mice
701 undergoing surgery were dosed with 1mg/kg buprenorphine sustained release formulation 1
702 hour before surgery. Right before surgery, mice were anesthetized with 3% isoflurane. The non-
703 surgical eye received artificial tears ointment (Covetrus #11695-6832-1. The surgical eye was
704 sterilized as described in the intravitreal injections section above. Topical anesthetic 0.5%
705 proparacaine HCl ophthalmic solution (Henry Schein #1365345) was applied on the surgical eye
706 (left). A pair of Vannas scissors (World Precision Instruments #501777) were used to make
707 incisions in the conjunctival layers. The optic nerve section in the intra-orbital space was exposed
708 by using two pairs of suture-tying forceps (Fine Science Tools #1106307) to gently clear the soft
709 tissue behind the eye until the optic nerve was visible. The optic nerve was manually crushed for
710 5s by using a pair of Dumont forceps (Fine Science Tools #1125325). The eyeball was gently

711 placed back into the orbit. Animals were post-surgically monitored in their home cages until
712 sternal recumbency was observed.
713
714 **Immunolabeling of retinae for cleaved caspase 3**
715 At the experimental endpoint (3 days after optic nerve crush) mice were euthanized by an
716 overdose of isoflurane and followed by decapitation. The eyes were enucleated and drop-fixed
717 in 4% paraformaldehyde for 1 hour. The retinae were dissected out in 1X phosphate-buffered
718 saline (PBS) and then blocked with blocking buffer (5% goat serum, 0.5% Triton X-100 and 0.025%
719 sodium azide in 1X PBS) for 30min. The retinae were then immersed in primary antibody solution
720 (anti-cleaved caspase 3, CST 9661) prepared by dilution in blocking buffer solution and incubated
721 for 5 days in 4°C. They were then washed three times in 1X PBS with 0.5% TritonX-100 for 30 min
722 each, and then moved to appropriate secondary antibody solution prepared in blocking buffer
723 and incubated overnight in 4°C. After secondary antibody incubation, they were washed again
724 three times in 1X PBS with 0.5% TritonX-100 for 30 min each. Retinae were then mounted in
725 Drop-n-Stain EverBrite^{TM} Mounting Medium (Biotium #23008) onto slides and imaged using Zeiss
726 Axio Imager Z1 fluorescence microscope. 5-8 images were taken per animal in a blinded manner
727 for quantification.
728
729 **Quantification of cleaved caspase 3-positive RGCs**
730 The number of cleaved caspase 3 positive cells were quantified in 5-8 images per retina per
731 animal in a blinded manner. The number of caspase 3 positive cells per section was averaged
732 over all the images quantified to obtain the average number of cleaved caspase 3 cells per
733 section.
734
735 **Retinal dissection for RBPMS analysis**
736 For RGC survival 7 days post injury, prior to fixation in 4% paraformaldehyde for 1 hour, a burn
737 signal was applied to the dorsal pole of enucleated eyeballs to maintain orientation. Retinas were
738 then carefully dissected as flat whole-mounts employing four radial cuts, with the deepest
739 incision previously marked at the dorsal pole. The flattened whole-mounts underwent an
740 additional hour of post-fixation in 4% PFA, followed by a gentle removal of vitreous using brushes.
741 Subsequently, they were kept in phosphate-buffered saline (PBS) for further processing.
742
743 **Immunofluorescence for RBPMS**
744 Retinal ganglion cells (RGCs) in whole-mount retinas were identified through immunodetection
745 of the RBPMS (RNA-binding protein with multiple splicing) protein. Initially, all retinas were
746 permeated (4 × 10 minutes) in PBS containing 0.5% Triton X-100 (Tx). The primary antibody
747 (rabbit anti-RBPMS, GeneTex #GTX118619) was diluted at 1:500 and incubated overnight with
748 shaking at room temperature in a blocking buffer (2% Normal Donkey Serum, 0.5% Tx in PBS).
749 Next, the retinas were washed and incubated overnight with the appropriate secondary antibody
750 (donkey anti-rabbit Alexa 649, Jackson ImmunoResearch, #706-495-148) diluted 1:500. Finally,
751 retinas were washed in PBS and cover-slipped vitreal side up with antifading mounting medium.
752
753 **Image acquisition**

754 RBPMS$^+$RGCs were imaged from flattened retinal whole-mounts using a 20x objective on an LSM
755 780 Zeiss confocal microscope equipped with a computer-driven motorized stage controlled by
756 Zen Lite software (Black edition, Zeiss). Photomontage frames were captured contiguously side-
757 by-side with an 8% overlap between them, and images within the same frame were acquired at
758 intervals of 3.5 microns in the Z-dimension. The maximum-projection images were employed for
759 subsequent analysis.
760
761 **Quantification of RBPMS RGCs**
762 Quantification of RBPMS$^+$RGCs was conducted on entire retinas using an automated algorithm in
763 ImageJ. Briefly, to minimize interference with background labeling, a rolling ball radius of 50
764 pixels was subtracted. The application of a median radius of 1 smoothed the edges, followed by
765 a maximum radius of 0.0005 to fill and dilate the objects. Subsequently, all images underwent an
766 8-bit grayscale transformation to eliminate color information, and a predetermined lower
767 threshold generate a binary mask-like images. The "watershed" segmentation automatically
768 separated particles that were in contact, while the "despeckle" median filter efficiently removed
769 noise. Positive objects were counted within defined parameters regarding shape and size, to
770 exclude those considered either too small or too large to be classified as RGCs. The automatic
771 routine extracted cell counts and their corresponding coordinates (x, y), which were exported to
772 a spreadsheet (Microsoft Office Excel; Microsoft Corp., Redmond, WA, USA) for further analysis
773 (see the next section).
774
775 **Spatial Analysis**
776 Topographical distributions of RBPMS$^+$RGC densities were assessed using color-filled contour
777 maps generated with Sigma Plot 13.0 for Windows (Systat Software, Inc., Richmond, CA, USA).
778 These heat maps assigned a color code to each area of interest (83.3 × 83.3 µm) based on its
779 density values, ranging from 0 (purple) to 3,600 RGCs/mm^2 (red) in a 10-step color scale.
780
781 **DLK inhibitor treatment**
782 GNE-3511 solution was synthesized as previously described [71]. Briefly, GNE-3511 was dissolved
783 in a solution of 0.5% w/v USP Grade Methyl Cellulose and 0.2% v/v Tween 80 in water up to 48
784 hours before dosing. Mice were dosed by oral gavage every 12 hours at 75 mg/kg with 10 ml/kg
785 body weight of a 7.5 mg/ml solution of GNE-3511 or vehicle alone.
786
787 **Statistical analyses**
788 All quantifications in this study (except for Western blots), were performed blind to experimental
789 groups and conditions. All statistical analysis was performed in GraphPad Prism 9 unless
790 otherwise stated.
791
792
793 **Funding**
794 This work was supported by NIH intramural funding NICHD ZIA-HD008966 (CLP), by a Milton-
795 Safenowitz postdoctoral fellowship from the ALS Association (JG-D), by NIH grant R01NS112691
796 (TAW) and grant #021-107 from Mission Connect, a project of the TIRR Foundation (TAW), and
797 NIH intramural funding NINDS 1ZIANS003155-03 (MEW) and NEI ZIAEY000488 (WL).

Acknowledgements

We would like to thank Drs. Vincent Schram and Chip Dye and the NICHD Microscopy core, Dr. Yan Li and the NINDS proteomics core, the NHLBI FACS core facility staff, Dr. Gareth Thomas (Temple University), Dr. Ana J. Garcia-Saez (Max Plank Institute of Biophysics) and Dr. Richard Cho (Cell Signaling Technologies) for reagents. We would also like to thank members of Dr. Michael Ward's lab for advice, and Dr. Nicholas Ryba, Dr. Richard Youle, Dr. David Simon, Dr. Alexander Chesler, and Dr. Joseph Lewcock for helpful discussion and comments on the manuscript.

Author contributions

Conceptualization: JGD and CLP.
Methodology and Investigation: all authors.
Formal Analysis: MN, FNN and JGD.
Visualization: JGD and CLP.
Writing: JGD and CLP.
Supervision: CLP, TW, LW, MEW.
Funding acquisition: CLP, TW, LW, MEW.

Figure 1: Axotomy triggers a wave of DRP1-dependent mitochondrial fission, axon degeneration and cell death

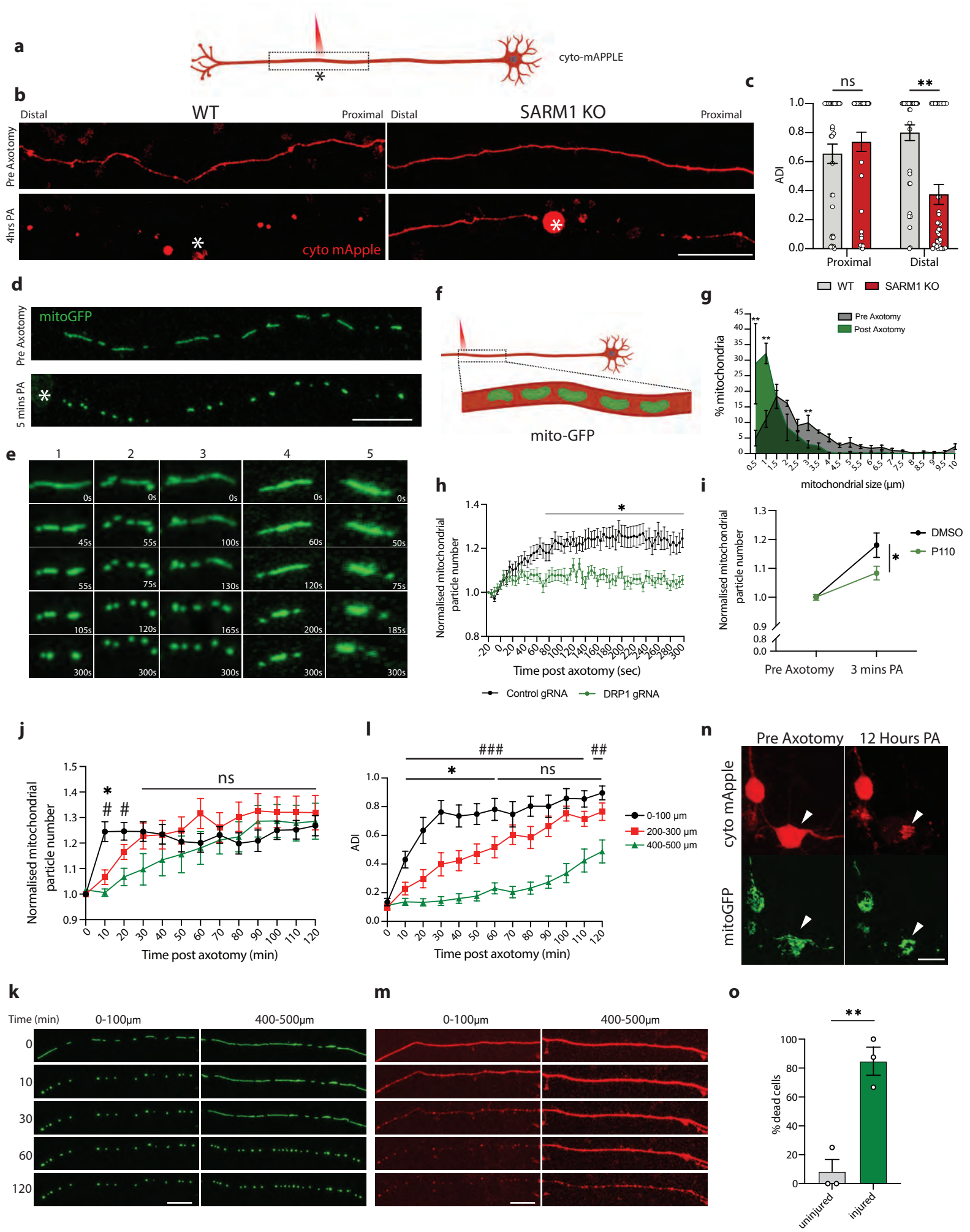

818 **Figure 1 – Axotomy triggers a wave of DRP1-dependent mitochondrial fission, axon**
819 **degeneration and cell death**
820
821 a) Schematic representation of i3Neuron laser axotomy using Biorender. Dashed box indicates
822 field of view. * Marks the site of axotomy
823 b) Representative images of WT and SARM1 KO axons transduced with cytoplasmic mApple
824 (red) pre and 4 hours post axotomy (PA). * Marks the site of axotomy. (Scale bar = 100 µm).
825 c) Quantification of axon degeneration index (ADI) in WT and SARM1 KO neurons distal and
826 proximal to the site of axon injury 4 hours post axotomy. Results are represented as mean ±
827 SEM. N=3 independent differentiations, N≥ 38 axons. Two-way ANOVA, Bonferroni correction
828 (p≤0.01 **, not significant, ns).
829 d) Representative images of i3Neuron axons transduced with mitoGFP (green) pre- and 5
830 minutes post axotomy (PA). * Marks the site of axotomy. (Scale bar = 20 µm). Time-lapse
831 images of mitochondria shown in E.
832 e) Representative images of mitochondria undergoing fission after axon injury outlined in D.
833 f) Schematic representation of i3Neuron laser axotomy. Dashed box indicates field of view.
834 g) Quantification of mitochondrial length pre (green) and 5 minutes post axotomy (grey) (PA).
835 Results are represented as mean ± SEM. N=3 independent differentiations, N≥ 28 axotomized
836 neurons. Two-way ANOVA, Bonferroni correction (p≤0.05 *).
837 h) Normalized number of mitochondrial particles post axotomy in control and DRP1 KD neurons.
838 Results are represented as mean ± SEM. N=3 independent differentiations, N≥ 25 axotomized
839 neurons. Two-way ANOVA, Bonferroni correction (p≤0.05 *).
840 i) Normalized number of mitochondrial particles 3 mins post axotomy in DMSO and P110
841 treated neurons. Results are represented as mean ± SEM. N=3 independent differentiations,
842 N≥ 26 axotomized neurons. Two-way ANOVA, Bonferroni correction (p≤0.05 *).
843 j) Quantification of axotomy-induced mitochondrial fission wave. Normalized number of
844 mitochondrial particles post axotomy 0-100, 200-300 and 400-500 µm from the site of
845 axotomy. Results are represented as mean ± SEM. N=3 independent differentiations, N≥ 23
846 axotomized neurons. One-way ANOVA, Bonferroni correction (*p≤0.05, 0-100 µm vs 200-300
847 µm, # p≤0.05, 0-100 µm vs 400-500 µm).
848 k) Representative images of axotomy-induced mitochondrial fission wave, Pre axotomy (0), 10-
849 , 30- and 120-minutes post axotomy. Neurons sparsely transduced with mitoGFP (green).
850 (Scale bar = 25 µm).
851 l) Quantification of axotomy-induced progressive axon degeneration. Axon degeneration index
852 (ADI) 0-100, 200-300 and 400-500µm from the site of axotomy. Results are represented as
853 mean ± SEM. N=3 independent differentiations, N≥ 14 axotomized neurons. (*p≤0.05, 0-100
854 µm vs 200-300 µm, ## p≤0.01, ### p≤0.005, 0-100 µm vs 400-500 µm).
855 m) Representative images of axotomy-induced axon degeneration. Pre axotomy (0), 10-, 30- and
856 120-minutes post axotomy. Neurons sparsely transduced with cyto-mApple (red). * Marks
857 the site of axotomy. (Scale bar = 25 µm).
858 n) Representative images of axotomy-induced neuron death. Pre and 12-hours post axotomy.
859 Arrow indicates axotomized neuron. Neurons sparsely transduced with cyto- mApple (red)
860 and mitoGFP (green). (Scale bar = 40 µm).

861 o) Quantification of axotomy-induced neuron death. Percentage of dead neurons 12 hours post
862 axotomy. Results are represented as mean ± SEM. N=3 independent differentiations, N≥30
863 axotomized neurons. Unpaired t-test ($p \leq 0.01$ **).
864

Figure 2: DLK regulates axotomy-induced mitochondrial fission

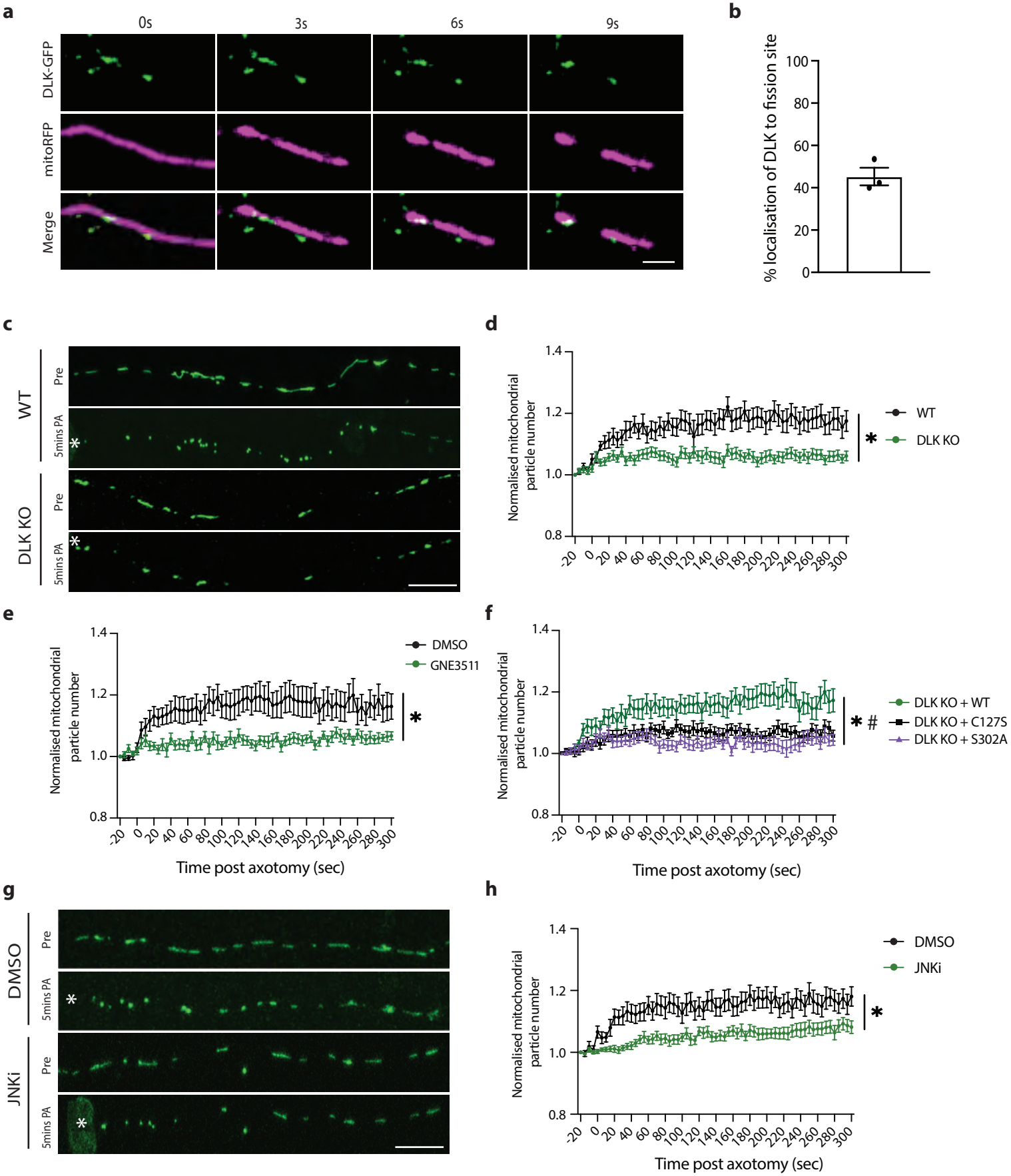

865 **Figure 2 – DLK regulates axotomy-induced mitochondrial fission**
866
867 a) Representative images of DLK colocalization at the site of mitochondrial fission after
868 axotomy. DLK-GFP (green) and mitochondria (mitoRFP, magenta). (Scale bar = 10 µm).
869 b) Percentage mitochondrial fission events where DLK is localized at the site of fission. Results
870 are represented as mean ± SEM. N=3 independent differentiations, N≥30 axotomized
871 neurons.
872 c) Representative images of WT and DLK KO neurons transduced with mitoGFP (green) pre (Pre)
873 and 5 mins post axotomy (PA). * Marks the site of axotomy. (Scale bar = 25 µm).
874 d) Normalized number of mitochondrial particles post axotomy in WT (black) and DLK KO (green)
875 neurons. Results are represented as mean ± SEM. N=3 independent differentiations, N≥ 30
876 axotomized neurons. (Two-way ANOVA, Bonferroni correction (p≤0.05 *)
877 e) Normalized number of mitochondrial particles post axotomy in DMSO (black) and GNE3511
878 (green)-treated neurons. Results are represented as mean ± SEM. N=3 independent
879 differentiations, N≥ 25 axotomized neurons. (Two-way ANOVA, Bonferroni correction (p≤0.05
880 *)
881 f) Normalized number of mitochondrial particles post axotomy in DLK KO neurons transduced
882 with WT DLK-GFP (green), DLK-C127S-GFP (black) or DLK-S302A-GFP (purple). Results are
883 represented as mean ± SEM. N=3 independent differentiations, N≥ 23 axotomized neurons.
884 Two-way ANOVA, Bonferroni correction (*p≤0.05, WT DLK vs DLK C127S, # p≤0.05, WT DLK vs
885 S302A).
886 g) Representative images of neurons transduced with mitoGFP (green) treated with DMSO and
887 JNKi pre (Pre) and 5 mins post axotomy (PA). * Marks the site of axotomy. (Scale bar = 25
888 µm).
889
890 h) Normalized number of mitochondrial particles post axotomy in DMSO (black) and JNKi
891 (green)-treated neurons. Results are represented as mean ± SEM. N=3 independent
892 differentiations, N≥ 30 axotomized neurons. (Two-way ANOVA, Bonferroni correction (p≤0.05
893 *)
894

Figure 3: Activation of the DLK pathway by overexpression causes increased DRP1 phopshorylation

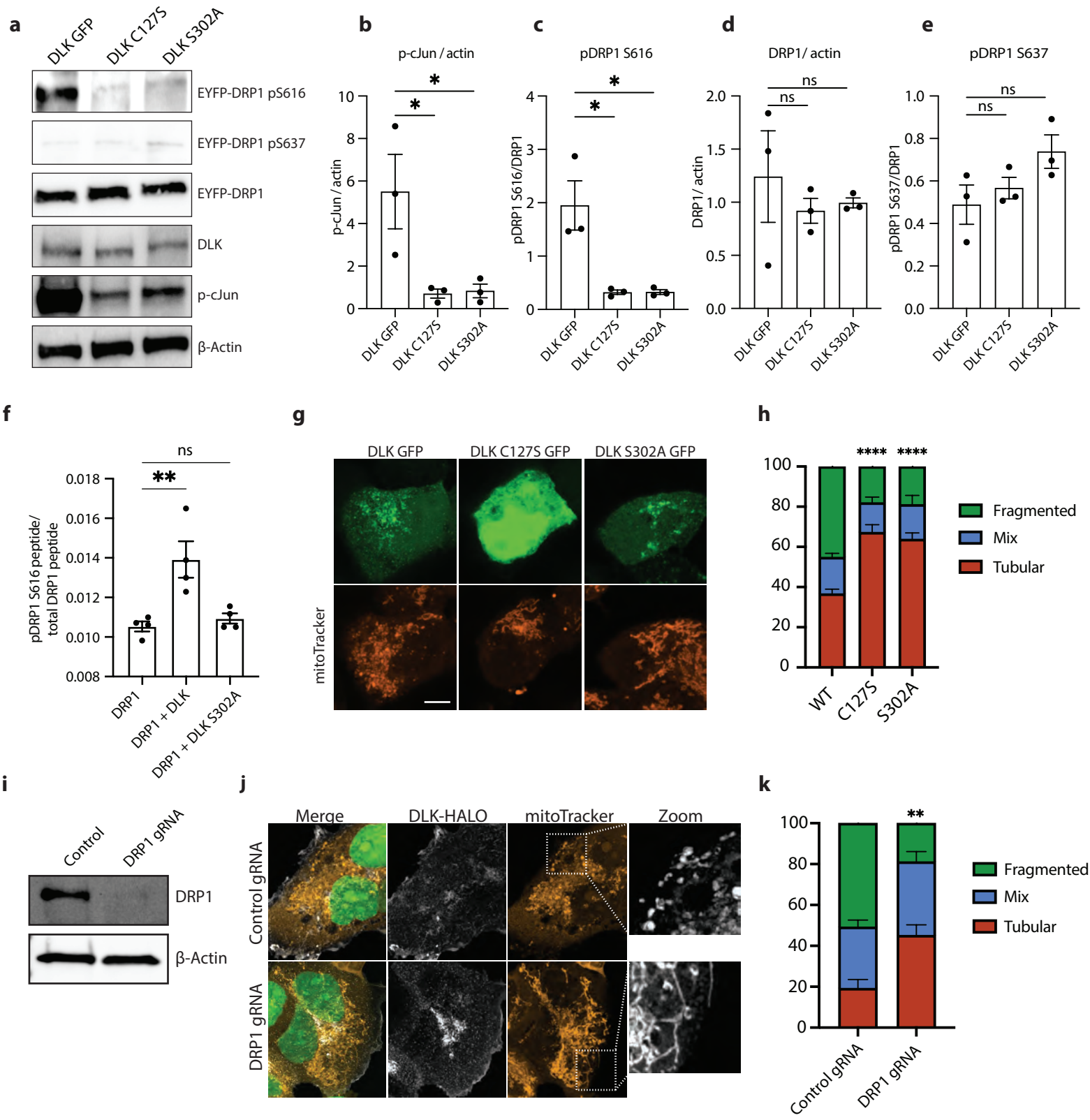

895 **Figure 3 – Activation of the DLK pathway by overexpression causes increased DRP1**
896 **phosphorylation**
897
898 a) Representative western blots of HEK293A cells transfected for 24 hours with WT, C127S and
899 S302A DLK-GFP. Immunoblot for pS616-DRP1, pS637-DRP1, total DRP1, DLK, pS63-cJun and
900 loading control ß actin.
901 b) Quantification of pS63-cJun/ ß actin levels after 24-hour expression of WT, C127S and S302A
902 DLK-GFP in HEK293A cells. Results are represented as mean ± SEM. One-way ANOVA,
903 Bonferroni correction (p≤0.05 *).
904 c) Quantification of pS616-DRP1/total DRP1 levels after 24-hour expression of WT, C127S and
905 S302A DLK-GFP in HEK293A cells. Results are represented as mean ± SEM. One-way ANOVA,
906 Bonferroni correction (p≤0.05 *).
907 d) Quantification of total DRP1/ ß actin levels after 24-hour expression of WT, C127S and S302A
908 DLK-GFP in HEK293A cells. Results are represented as mean ± SEM. One-way ANOVA,
909 Bonferroni correction (not significant, ns).
910 e) Quantification of pS637 DRP1/ ß actin levels after 24-hour expression of WT, C127S and
911 S302A DLK-GFP in HEK293A cells. Results are represented as mean ± SEM. One-way ANOVA,
912 Bonferroni correction (not significant, ns).
913 f) Phospho-mass spectrometry. pS616-DRP1 peptide / total DRP1 peptide levels from purified
914 GST-DRP1 in HEK 293A cells expressing GST-DRP1, GST-DRP1 and DLK-GFP or GST-DRP1 and
915 DLK-S302A-GFP. Results are represented as mean ± SEM. One-way ANOVA, Bonferroni
916 correction (p≤0.01 **).
917 g) Representative images of HEK-293A cells expressing WT, C127S and S302A DLK-GFP (green)
918 and mitoTracker (orange) for 24 hours. (Scale bar = 10 µm).
919 h) Quantification of mitochondrial morphology in HEK293A cells transfected for 24 hours with
920 WT, C127S and S302A DLK-GFP. N=3 individual transfections. Results are represented as
921 mean ± SEM. Two-way ANOVA, Bonferroni correction (WT vs C127S p≤0.0001 ****, WT vs
922 S302A p≤0.0001 ****, C127S vs S302A not significant, ns).
923 i) Representative western blots HEK-293A cells expressing dCAS9 transduced with control and
924 DRP1 gRNAs. Immunoblot for total DRP1 and loading control ß actin.
925 j) Representative images of Control and DRP1 KD HEK-293A cells expressing DLK-HALO for 24
926 hours. NLS-GFP (green), DLK-HALO (white), mitoTracker (orange). (Scale bar = 10 µm).
927 k) Quantification of Control and DRP1 KD HEK-293A cells mitochondrial morphology. Cells
928 transfected for 24 hours with DLK-HALO. N=3 individual transfections. Results are
929 represented as mean ± SEM. (Two-way ANOVA, Bonferroni correction (p≤0.01 **)
930

Figure 4: Axotomy causes DLK-dependent phosphorylation of DRP1

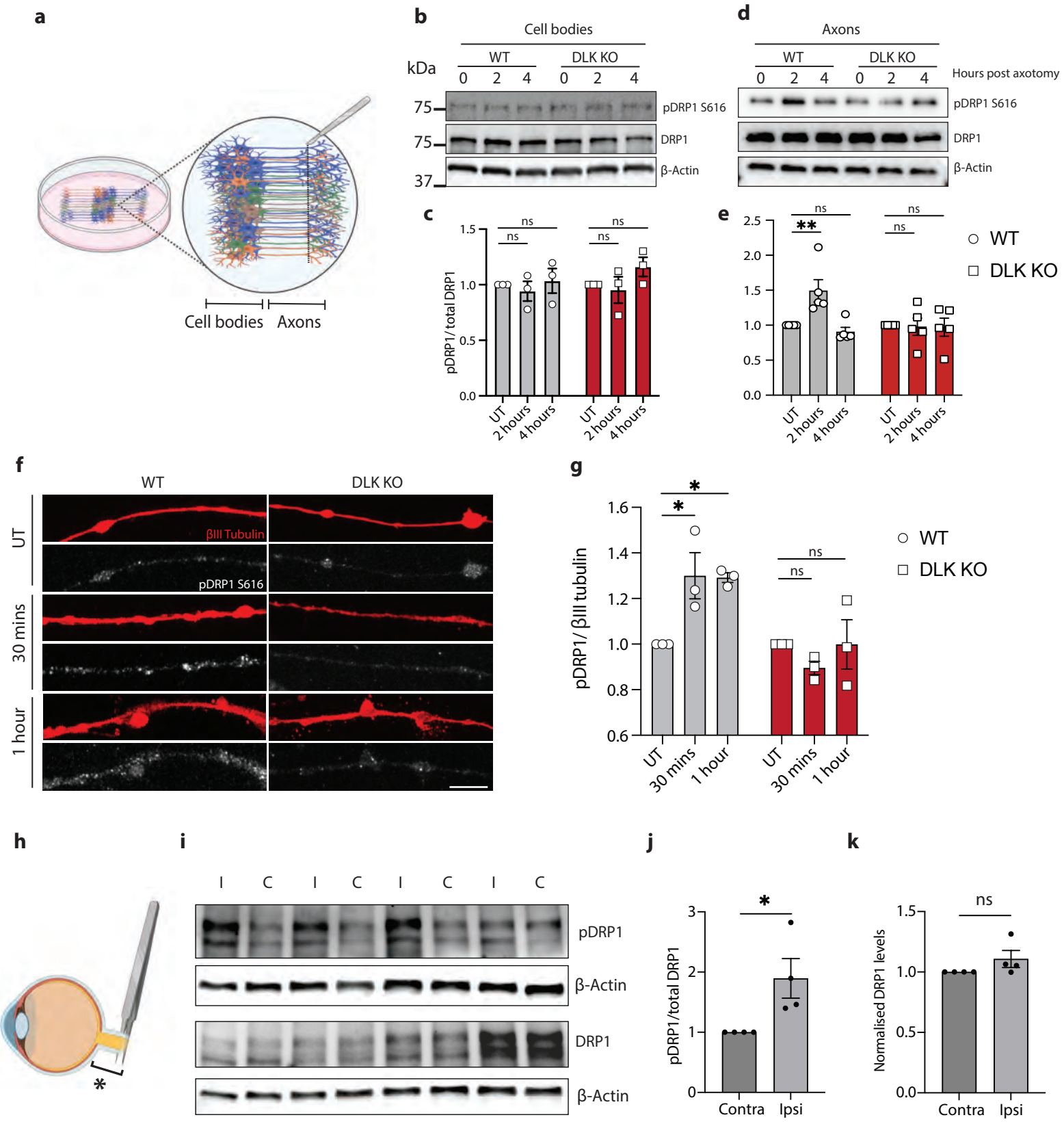

931 **Figure 4 – Axotomy causes DLK-dependent phosphorylation of DRP1**
932
933 a) Schematic representation of i3Neuron center plating and axotomy for protein harvesting
934 after injury.
935 b) Representative western blots of WT and DLK KO neuron cell bodies untreated (UT), 2 and 4
936 hours post axotomy. Immunoblot for p-S616 DRP1, total DRP1 and loading control ß actin.
937 c) Quantification of pDRP1 (S616)/ total DRP1 levels in WT and DLK KO neuron cell bodies
938 untreated (UT), 2 and 4 hours post axotomy. Results normalized to UT. Results are
939 represented as mean ± SEM. N=3 independent differentiations. One-way ANOVA. No
940 significant changes observed.
941 d) Representative western blots of WT and DLK KO neuron axons untreated (UT), 2 and 4 hours
942 post axotomy. Immunoblot for p-S616 DRP1, total DRP1 and loading control ß actin.
943 e) Quantification of pDRP1 (S616)/ total DRP1 levels in WT and DLK KO neuron axons 0, 2 and 4
944 hours post axotomy. Results normalized to UT. Results are represented as mean ± SEM. N=3
945 independent differentiations. Two-way ANOVA. Bonferroni correction ($p \leq 0.05$*).
946 f) Representative images of WT and DLK KO axons stained for ßIII tubulin (red) and pDRP1 S616
947 (white) untreated (UT), 30 mins and 1 hour post axotomy. (Scale bar = 25 µm).
948 g) Quantification of pDRP1 S616 fluorescence in WT and DLK KO neuron axons after axotomy.
949 Results normalized to untreated axons. Results are represented as mean ± SEM. N=3
950 independent differentiations. Two-way ANOVA, Bonferroni correction ($p \leq 0.05$ *)
951 h) Schematic representation of optic nerve crush injury model. Bracket and * indicate the
952 proximal portion of the injured nerve harvested for western blotting.
953 i) Representative western blots of proximal portion of ipsilateral (I) injured and contralateral
954 (C) optic nerves 24 hours after optic nerve crush. Immunoblot for p-S616 DRP1, total DRP1
955 and loading control ß actin.
956 j) Quantification of pDRP1 (S616)/ total DRP1 levels after optic nerve crush. Results normalized
957 to contralateral side (C). Results are represented as mean ± SEM. Unpaired t-test ($p \leq 0.05$ *).
958 k) Quantification of total DRP1/ ß actin levels after optic nerve crush. Results normalized to
959 contralateral side (C). Results are represented as mean ± SEM. Unpaired t-test not significant,
960 ns.
961

Figure 5: Blocking DRP1 or DLK delays axonal degeneration

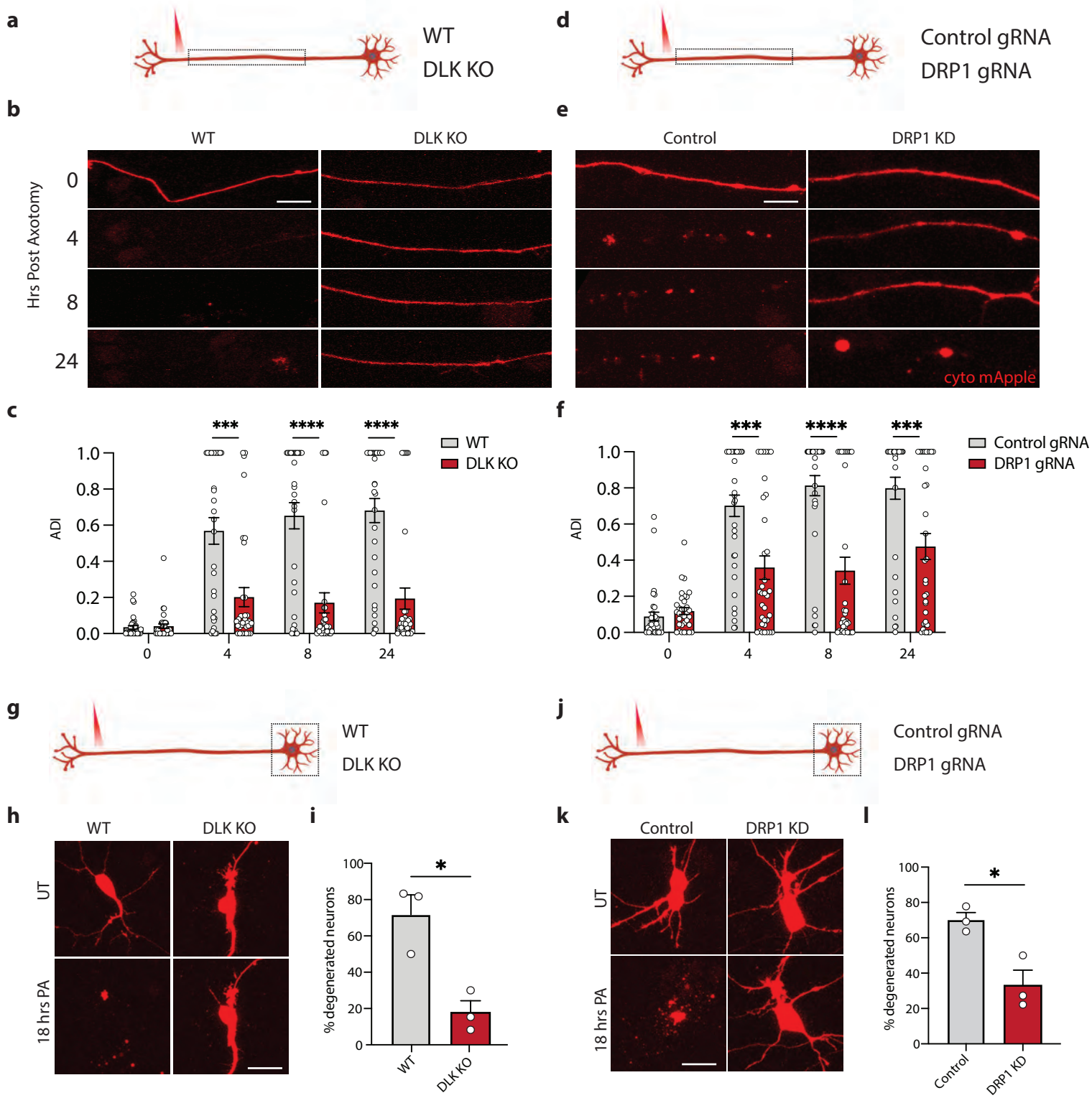

962 **Figure 5 – Blocking DRP1 or DLK delays axon degeneration**
963
964 a) Schematic representation of i3Neuron laser axotomy. Dashed box indicates the field of view
965 b) Representative images of WT and DLK KO neuron axons transduced with cyto mApple (red)
966 proximal to the site of injury 0,4, 8 and 24 hours post axotomy (Scale bar = 25 µm).
967 c) Quantification of axon degeneration index (ADI) in WT and DLK KO neurons 0, 4, 8 and 24
968 hours post axotomy. Results are represented as mean ± SEM. N=3 independent
969 differentiations, N≥ 33 axons. Two-way ANOVA, Bonferroni correction (p≤0.005 ***, p≤0.001
970 ****).
971 d) Schematic representation of i3Neuron laser axotomy. Dashed box indicates field of view.
972 e) Representative images of Control and DRP1 KD neuron axons transduced with cyto mApple
973 (red) proximal to the site of injury 0, 4, 8 and 24 hours post axotomy (Scale bar = 25 µm).
974 f) Quantification of axon degeneration index (ADI) in WT and DLK KO neurons 0, 4, 8 and 24
975 hours post axotomy. Results are represented as mean ± SEM. N=3 independent
976 differentiations, N≥ 33 axons. Two-way ANOVA, Bonferroni correction (p≤0.005 ***, p≤0.001
977 ****).
978 g) Schematic representation of i3Neuron laser axotomy. Dashed box indicates field of view.
979 h) Representative images of WT and DLK KO neuron cell bodies transduced with cyto mApple
980 (red) pre and 18 hours post axotomy (PA). (Scale bar = 40 µm).
981 i) Percentage degenerated WT and DLK KO 18 post axotomy. Results are represented as mean
982 ± SEM. N=3 independent differentiations. Unpaired t-test (p≤0.05 *).
983 j) Schematic representation of i3Neuron laser axotomy. Dashed box indicates field of view.
984 k) Representative images of Control and DRP1 KD neuron cell bodies transduced with cyto
985 mApple (red) pre and 18 hours post axotomy (PA). (Scale bar = 40 µm).
986 l) Percentage degenerated Control and DRP1 KD 18 post axotomy. Results are represented as
987 mean ± SEM. N=3 independent differentiations. Unpaired t-test (p≤0.05 *).
988
989

Fig 6: DRP1 mediates cell death after ONC

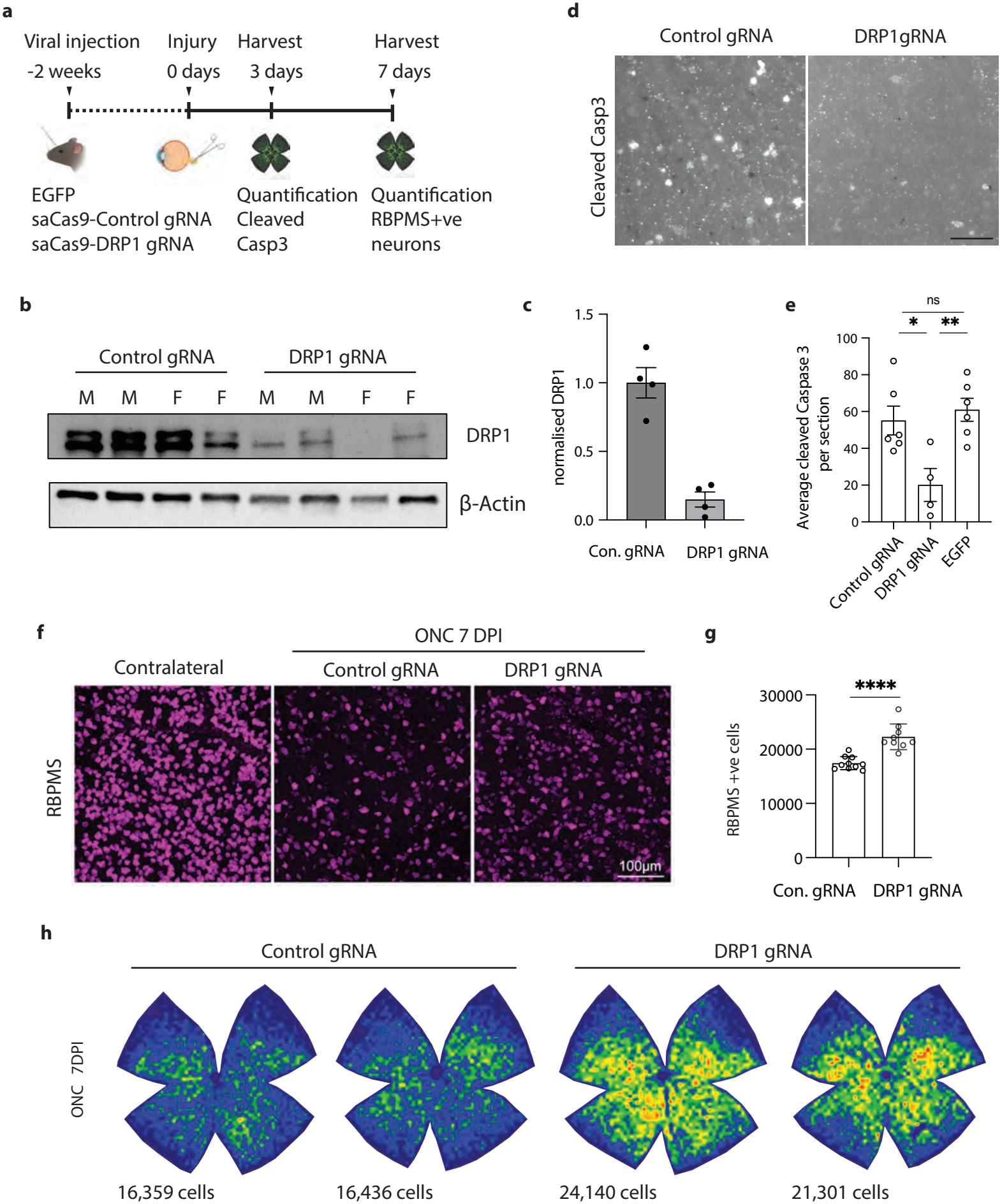

Figure 6 – DRP1 mediates cell death after ONC

a) Schematic representation of RGC survival following optic nerve crush (ONC).
b) Western blots of Control and DRP1 gRNA transduced optic nerved. Immunoblot for DRP1 and loading control ß actin.
c) Quantification of DRP1 knockdown by Western blot. Results are represented as mean ± SEM.
d) Representative images of cleaved caspase 3 positive cells in saCas9-Control and saCas9-DRP1 gRNA transduced RGCs 3 days after ONC. (Scale bar = 25 µm).
e) Average cleaved caspase 3 positive cells per section in saCas9-Control, saCas9-DRP1 gRNA and EGFP transduced RGCs after nerve crush. Results are represented as mean ± SEM. N≥4 animals per condition. One-way ANOVA, Bonferroni correction. (Control gRNA vs EGFP, not significant, ns. Control gRNA vs DRP1 gRNA $p \leq 0.05$ *. DRP1 gRNA vs EGFP $p \leq 0.01$ **).
f) Representative images of retinas 7 days post ONC and immunostained for RGC marker RBPMS (magenta). Images acquired at similar areas and the same distance from the optic nerve head (ONH). Scale bar = 100 µm.
g) Quantification of RBPMS-positive RGCs in the retinas of control and DRP1 gRNA mice at 7DPI. (N=8 mice per condition. Unpaired t-test $P < 0.0001$ ****)
h) Representative isodensity maps display the topographical survival of RBPMS+RGCs at 7 days post-injury. DRP1 gRNA treatment delays ONC-induced RGC degeneration across the retina. Color scale for isodensity maps ranges from 0 (purple) to 3,600 (red) RGCs/mm².

Fig 7: BAX mediates cell death after axotomy

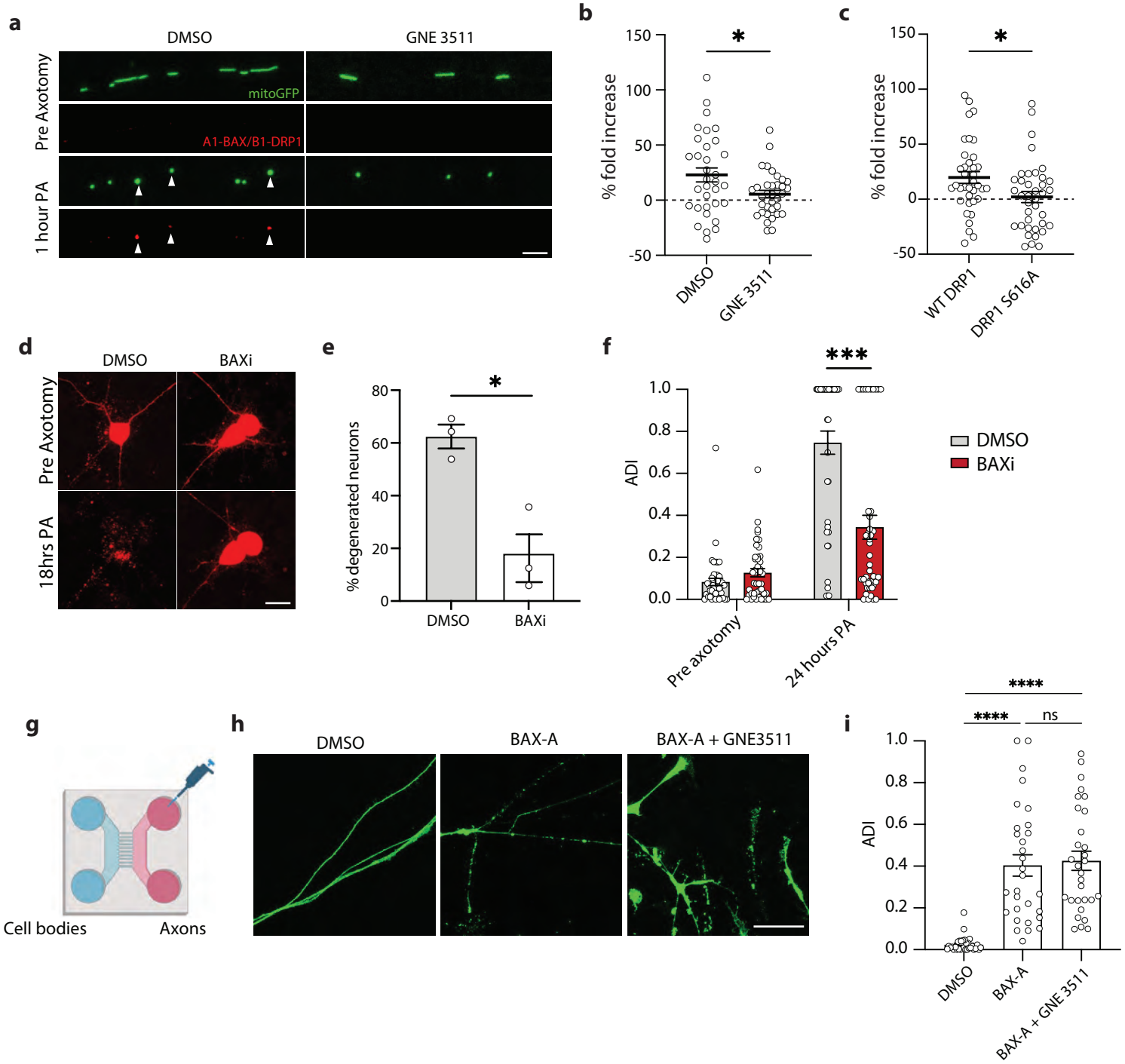

1013 **Figure 7 – BAX regulates cell death after axotomy**
1014
1015 a) Representative images of WT neurons treated with DMSO or GNE3511 pre- and 1-hour post-
1016 axotomy (PA) expressing mitoGFP (green) and A_1-BAX/B_1-DRP1 complexes (red). (Scale bar =
1017 5 µm).
1018 b) Quantification of A_1-BAX/B_1-DRP1 fluorescence fold change in the mitochondria of DMSO or
1019 GNE3511 treated neurons 1-hour post-axotomy. Results are represented as mean ± SEM. N=3
1020 independent differentiations, N≥ 34 axotomized neurons. Two-way ANOVA, Bonferroni
1021 correction. ($p \leq 0.05$ *).
1022 c) Quantification of A_1-BAX/B_1- WT DRP1 and A_1-BAX/B_1- DRP1 S616A fluorescence fold change
1023 in the mitochondria 1-hour post-axotomy. Results are represented as mean ± SEM. N=3
1024 independent differentiations, N≥ 34 axotomized neurons. Two-way ANOVA, Bonferroni
1025 correction. ($p \leq 0.05$ *).
1026 d) Representative images of DMSO and BAXi treated neuron cell bodies transduced with cyto
1027 mApple (red) pre and 18 hours post axotomy (PA). (Scale bar = 40 µm).
1028 e) Percent degenerated neurons 18 hours post axotomy treated with either DMSO or BAXi.
1029 Results are represented as mean ± SEM. N=3 independent differentiations. Unpaired t-test
1030 ($p \leq 0.05$ *).
1031 f) Quantification of axon degeneration index (ADI) of DMSO and BAX-A-treated neurons 24
1032 hours after axotomy. Results are represented as mean ± SEM. N=3 independent
1033 differentiations. One-way ANOVA, Bonferroni correction ($p \leq 0.001$ ***, not significant, ns).
1034 g) Illustration of microfluidic devices used to separate axons from somas allowing for the local
1035 treatment of i3Neuron axons.
1036 h) Representative images of WT axons separated using microfluidic chambers treated with
1037 DMSO, BAX-A or BAX-A + GNE3511 for 24 hours. (Scale bar = 25 µm).
1038 i) Quantification of axon degeneration index (ADI) of isolated axons treated with DMSO BAX-A
1039 and BAX-A + GNE3511 for 24 hours. Results are represented as mean ± SEM. N=3 independent
1040 differentiations. One-way ANOVA, Bonferroni correction ($p \leq 0.001$ ****, not significant, ns).
1041
1042

1043 **References**
1044

1045 1. Whitmore, A.V., et al., *The proapoptotic proteins Bax and Bak are not involved in*
1046 *Wallerian degeneration.* Cell Death Differ, 2003. **10**(2): p. 260-1.
1047 2. Deckwerth, T.L., et al., *BAX is required for neuronal death after trophic factor deprivation*
1048 *and during development.* Neuron, 1996. **17**(3): p. 401-11.
1049 3. Simon, D.J., et al., *Axon Degeneration Gated by Retrograde Activation of Somatic Pro-*
1050 *apoptotic Signaling.* Cell, 2016. **164**(5): p. 1031-45.
1051 4. Simon, D.J., et al., *A caspase cascade regulating developmental axon degeneration.* J
1052 Neurosci, 2012. **32**(49): p. 17540-53.
1053 5. Osterloh, J.M., et al., *dSarm/Sarm1 is required for activation of an injury-induced axon*
1054 *death pathway.* Science, 2012. **337**(6093): p. 481-4.
1055 6. Gerdts, J., et al., *SARM1 activation triggers axon degeneration locally via NAD(+)*
1056 *destruction.* Science, 2015. **348**(6233): p. 453-7.
1057 7. Peters, O.M., et al., *Loss of Sarm1 does not suppress motor neuron degeneration in the*
1058 *SOD1G93A mouse model of amyotrophic lateral sclerosis.* Hum Mol Genet, 2018. **27**(21):
1059 p. 3761-3771.
1060 8. Fernandes, K.A., et al., *Role of SARM1 and DR6 in retinal ganglion cell axonal and somal*
1061 *degeneration following axonal injury.* Exp Eye Res, 2018. **171**: p. 54-61.
1062 9. Mandal, A. and C.M. Drerup, *Axonal Transport and Mitochondrial Function in Neurons.*
1063 Front Cell Neurosci, 2019. **13**: p. 373.
1064 10. Smith, G.M. and G. Gallo, *The role of mitochondria in axon development and regeneration.*
1065 Dev Neurobiol, 2018. **78**(3): p. 221-237.
1066 11. Han, S.M., H.S. Baig, and M. Hammarlund, *Mitochondria Localize to Injured Axons to*
1067 *Support Regeneration.* Neuron, 2016. **92**(6): p. 1308-1323.
1068 12. Lin, M.Y., et al., *Releasing Syntaphilin Removes Stressed Mitochondria from Axons*
1069 *Independent of Mitophagy under Pathophysiological Conditions.* Neuron, 2017. **94**(3): p.
1070 595-610 e6.
1071 13. Karbowski, M. and R.J. Youle, *Dynamics of mitochondrial morphology in healthy cells and*
1072 *during apoptosis.* Cell Death Differ, 2003. **10**(8): p. 870-80.
1073 14. Espinos, C., V. Felipo, and F. Palau, *Inherited neuromuscular diseases. Translation from*
1074 *pathomechanisms to therapies.* Adv Exp Med Biol, 2009. **652**: p. v-vi.
1075 15. Tilokani, L., et al., *Mitochondrial dynamics: overview of molecular mechanisms.* Essays
1076 Biochem, 2018. **62**(3): p. 341-360.
1077 16. Youle, R.J. and A.M. van der Bliek, *Mitochondrial fission, fusion, and stress.* Science, 2012.
1078 **337**(6098): p. 1062-5.
1079 17. Lee, Y.J., et al., *Roles of the mammalian mitochondrial fission and fusion mediators Fis1,*
1080 *Drp1, and Opa1 in apoptosis.* Mol Biol Cell, 2004. **15**(11): p. 5001-11.
1081 18. Frank, S., et al., *The role of dynamin-related protein 1, a mediator of mitochondrial fission,*
1082 *in apoptosis.* Dev Cell, 2001. **1**(4): p. 515-25.
1083 19. Jenner, A., et al., *DRP1 interacts directly with BAX to induce its activation and apoptosis.*
1084 EMBO J, 2022. **41**(8): p. e108587.
1085 20. Milani, M., et al., *DRP-1 functions independently of mitochondrial structural perturbations*
1086 *to facilitate BH3 mimetic-mediated apoptosis.* Cell Death Discov, 2019. **5**: p. 117.

1087 21. Tian, R., et al., *CRISPR Interference-Based Platform for Multimodal Genetic Screens in*
1088 *Human iPSC-Derived Neurons.* Neuron, 2019. **104**(2): p. 239-255 e12.
1089 22. Liao, Y.C., et al., *RNA Granules Hitchhike on Lysosomes for Long-Distance Transport, Using*
1090 *Annexin A11 as a Molecular Tether.* Cell, 2019. **179**(1): p. 147-164 e20.
1091 23. Goldsmith, J., et al., *Brain-derived autophagosome profiling reveals the engulfment of*
1092 *nucleoid-enriched mitochondrial fragments by basal autophagy in neurons.* Neuron, 2024.
1093 **112**(3): p. 520.
1094 24. Fernandopulle, M.S., et al., *Transcription Factor-Mediated Differentiation of Human iPSCs*
1095 *into Neurons.* Curr Protoc Cell Biol, 2018. **79**(1): p. e51.
1096 25. Zhang, Y., et al., *Rapid single-step induction of functional neurons from human pluripotent*
1097 *stem cells.* Neuron, 2013. **78**(5): p. 785-98.
1098 26. Miller, B.R., et al., *A dual leucine kinase-dependent axon self-destruction program*
1099 *promotes Wallerian degeneration.* Nat Neurosci, 2009. **12**(4): p. 387-9.
1100 27. Huntwork-Rodriguez, S., et al., *JNK-mediated phosphorylation of DLK suppresses its*
1101 *ubiquitination to promote neuronal apoptosis.* J Cell Biol, 2013. **202**(5): p. 747-63.
1102 28. Larhammar, M., et al., *Dual leucine zipper kinase-dependent PERK activation contributes*
1103 *to neuronal degeneration following insult.* Elife, 2017. **6**.
1104 29. Le Pichon, C.E., et al., *Loss of dual leucine zipper kinase signaling is protective in animal*
1105 *models of neurodegenerative disease.* Sci Transl Med, 2017. **9**(403).
1106 30. Asghari Adib, E., L.J. Smithson, and C.A. Collins, *An axonal stress response pathway:*
1107 *degenerative and regenerative signaling by DLK.* Curr Opin Neurobiol, 2018. **53**: p. 110-
1108 119.
1109 31. Ferraris, D., Z. Yang, and D. Welsbie, *Dual leucine zipper kinase as a therapeutic target for*
1110 *neurodegenerative conditions.* Future Med Chem, 2013. **5**(16): p. 1923-34.
1111 32. Siu, M., A. Sengupta Ghosh, and J.W. Lewcock, *Dual Leucine Zipper Kinase Inhibitors for*
1112 *the Treatment of Neurodegeneration.* J Med Chem, 2018. **61**(18): p. 8078-8087.
1113 33. Welsbie, D.S., et al., *Enhanced Functional Genomic Screening Identifies Novel Mediators*
1114 *of Dual Leucine Zipper Kinase-Dependent Injury Signaling in Neurons.* Neuron, 2017. **94**(6):
1115 p. 1142-1154 e6.
1116 34. Franco, A., et al., *Mitochondrial Dysfunction and Pharmacodynamics of Mitofusin*
1117 *Activation in Murine Charcot-Marie-Tooth Disease Type 2A.* J Pharmacol Exp Ther, 2022.
1118 **383**(2): p. 137-148.
1119 35. Taylor, A.M., et al., *A microfluidic culture platform for CNS axonal injury, regeneration and*
1120 *transport.* Nat Methods, 2005. **2**(8): p. 599-605.
1121 36. Watkins, T.A., et al., *DLK initiates a transcriptional program that couples apoptotic and*
1122 *regenerative responses to axonal injury.* Proc Natl Acad Sci U S A, 2013. **110**(10): p. 4039-
1123 44.
1124 37. Gomez-Deza, J., et al., *Local production of reactive oxygen species drives vincristine-*
1125 *induced axon degeneration.* Cell Death Dis, 2023. **14**(12): p. 807.
1126 38. Court, F.A. and M.P. Coleman, *Mitochondria as a central sensor for axonal degenerative*
1127 *stimuli.* Trends Neurosci, 2012. **35**(6): p. 364-72.
1128 39. Wang, B., et al., *Mitochondrial Behavior in Axon Degeneration and Regeneration.* Front
1129 Aging Neurosci, 2021. **13**: p. 650038.

1130 40. George, E.B., J.D. Glass, and J.W. Griffin, *Axotomy-induced axonal degeneration is*
1131 *mediated by calcium influx through ion-specific channels.* J Neurosci, 1995. **15**(10): p.
1132 6445-52.
1133 41. Villegas, R., et al., *Calcium release from intra-axonal endoplasmic reticulum leads to axon*
1134 *degeneration through mitochondrial dysfunction.* J Neurosci, 2014. **34**(21): p. 7179-89.
1135 42. Farley, M.M. and T.A. Watkins, *Intrinsic Neuronal Stress Response Pathways in Injury and*
1136 *Disease.* Annu Rev Pathol, 2018. **13**: p. 93-116.
1137 43. Holland, S.M., et al., *Palmitoylation controls DLK localization, interactions and activity to*
1138 *ensure effective axonal injury signaling.* Proc Natl Acad Sci U S A, 2016. **113**(3): p. 763-8.
1139 44. Nihalani, D., S. Merritt, and L.B. Holzman, *Identification of structural and functional*
1140 *domains in mixed lineage kinase dual leucine zipper-bearing kinase required for complex*
1141 *formation and stress-activated protein kinase activation.* J Biol Chem, 2000. **275**(10): p.
1142 7273-9.
1143 45. Archer, S.L., *Mitochondrial dynamics--mitochondrial fission and fusion in human diseases.*
1144 N Engl J Med, 2013. **369**(23): p. 2236-51.
1145 46. Ghosh, A.S., et al., *DLK induces developmental neuronal degeneration via selective*
1146 *regulation of proapoptotic JNK activity.* J Cell Biol, 2011. **194**(5): p. 751-64.
1147 47. Yu, R., et al., *The phosphorylation status of Ser-637 in dynamin-related protein 1 (Drp1)*
1148 *does not determine Drp1 recruitment to mitochondria.* J Biol Chem, 2019. **294**(46): p.
1149 17262-17277.
1150 48. Chang, C.R. and C. Blackstone, *Cyclic AMP-dependent protein kinase phosphorylation of*
1151 *Drp1 regulates its GTPase activity and mitochondrial morphology.* J Biol Chem, 2007.
1152 **282**(30): p. 21583-7.
1153 49. Hunker, A.C., et al., *Conditional Single Vector CRISPR/SaCas9 Viruses for Efficient*
1154 *Mutagenesis in the Adult Mouse Nervous System.* Cell Rep, 2020. **30**(12): p. 4303-4316 e6.
1155 50. Robitaille, K., et al., *Calphostin C-induced apoptosis is mediated by a tissue*
1156 *transglutaminase-dependent mechanism involving the DLK/JNK signaling pathway.* Cell
1157 Death Differ, 2008. **15**(9): p. 1522-31.
1158 51. Karbowski, M., et al., *Spatial and temporal association of Bax with mitochondrial fission*
1159 *sites, Drp1, and Mfn2 during apoptosis.* J Cell Biol, 2002. **159**(6): p. 931-8.
1160 52. Alford, S.C., et al., *A fluorogenic red fluorescent protein heterodimer.* Chem Biol, 2012.
1161 **19**(3): p. 353-60.
1162 53. Garner, T.P., et al., *Small-molecule allosteric inhibitors of BAX.* Nat Chem Biol, 2019. **15**(4):
1163 p. 322-330.
1164 54. Cosker, K.E., et al., *Target-derived neurotrophins coordinate transcription and transport*
1165 *of bclw to prevent axonal degeneration.* J Neurosci, 2013. **33**(12): p. 5195-207.
1166 55. Reyna, D.E., et al., *Direct Activation of BAX by BTSA1 Overcomes Apoptosis Resistance in*
1167 *Acute Myeloid Leukemia.* Cancer Cell, 2017. **32**(4): p. 490-505 e10.
1168 56. Donahue, R.J., et al., *BAX-Depleted Retinal Ganglion Cells Survive and Become Quiescent*
1169 *Following Optic Nerve Damage.* Mol Neurobiol, 2020. **57**(2): p. 1070-1084.
1170 57. Goldenberg-Cohen, N., et al., *Protective effect of Bax ablation against cell loss in the*
1171 *retinal ganglion layer induced by optic nerve crush in transgenic mice.* J Neuroophthalmol,
1172 2011. **31**(4): p. 331-8.

1173 58. Kedra, J., et al., *Axotomy Induces Drp1-Dependent Fragmentation of Axonal Mitochondria.*
1174 Front Mol Neurosci, 2021. **14**: p. 668670.
1175 59. Barrientos, S.A., et al., *Axonal degeneration is mediated by the mitochondrial permeability*
1176 *transition pore.* J Neurosci, 2011. **31**(3): p. 966-78.
1177 60. Cavanagh, J.B., *The significance of the "dying back" process in experimental and human*
1178 *neurological disease.* Int Rev Exp Pathol, 1964. **3**: p. 219-67.
1179 61. Yaron, A. and O. Schuldiner, *Common and Divergent Mechanisms in Developmental*
1180 *Neuronal Remodeling and Dying Back Neurodegeneration.* Curr Biol, 2016. **26**(13): p.
1181 R628-R639.
1182 62. Coleman, M., *Axon degeneration mechanisms: commonality amid diversity.* Nat Rev
1183 Neurosci, 2005. **6**(11): p. 889-98.
1184 63. Coleman, M.P., *Axon Biology in ALS: Mechanisms of Axon Degeneration and Prospects for*
1185 *Therapy.* Neurotherapeutics, 2022. **19**(4): p. 1133-1144.
1186 64. Geisler, S., et al., *Vincristine and bortezomib use distinct upstream mechanisms to activate*
1187 *a common SARM1-dependent axon degeneration program.* JCI Insight, 2019. **4**(17).
1188 65. White, M.A., et al., *Sarm1 deletion suppresses TDP-43-linked motor neuron degeneration*
1189 *and cortical spine loss.* Acta Neuropathol Commun, 2019. **7**(1): p. 166.
1190 66. Yang, J., et al., *Pathological axonal death through a MAPK cascade that triggers a local*
1191 *energy deficit.* Cell, 2015. **160**(1-2): p. 161-76.
1192 67. Guo, X., et al., *Inhibition of mitochondrial fragmentation diminishes Huntington's disease-*
1193 *associated neurodegeneration.* J Clin Invest, 2013. **123**(12): p. 5371-88.
1194 68. Joshi, A.U., et al., *Inhibition of Drp1/Fis1 interaction slows progression of amyotrophic*
1195 *lateral sclerosis.* EMBO Mol Med, 2018. **10**(3).
1196 69. Chen, Z., et al., *Inhibiting mitochondrial fission rescues degeneration in hereditary spastic*
1197 *paraplegia neurons.* Brain, 2022. **145**(11): p. 4016-4031.
1198 70. Flippo, K.H., et al., *Deletion of a Neuronal Drp1 Activator Protects against Cerebral*
1199 *Ischemia.* J Neurosci, 2020. **40**(15): p. 3119-3129.
1200 71. Patel, S., et al., *Discovery of dual leucine zipper kinase (DLK, MAP3K12) inhibitors with*
1201 *activity in neurodegeneration models.* J Med Chem, 2015. **58**(1): p. 401-18.
1202 72. Katz, J.S., et al., *A Phase 1 study of GDC-0134, a dual leucine zipper kinase inhibitor, in ALS.*
1203 Ann Clin Transl Neurol, 2022. **9**(1): p. 50-66.
1204 73. Chen, L., et al., *Mitochondria and Caspases Tune Nmnat-Mediated Stabilization to*
1205 *Promote Axon Regeneration.* PLoS Genet, 2016. **12**(12): p. e1006503.
1206 74. Kiryu-Seo, S. and H. Kiyama, *Mitochondrial behavior during axon*
1207 *regeneration/degeneration in vivo.* Neurosci Res, 2019. **139**: p. 42-47.
1208 75. Jahani-Asl, A., et al., *CDK5 phosphorylates DRP1 and drives mitochondrial defects in*
1209 *NMDA-induced neuronal death.* Hum Mol Genet, 2015. **24**(16): p. 4573-83.
1210 76. Rong, R., et al., *Cdk5-mediated Drp1 phosphorylation drives mitochondrial defects and*
1211 *neuronal apoptosis in radiation-induced optic neuropathy.* Cell Death Dis, 2020. **11**(9): p.
1212 720.
1213 77. Chen, S., et al., *TBK1-Mediated DRP1 Targeting Confers Nucleic Acid Sensing to Reprogram*
1214 *Mitochondrial Dynamics and Physiology.* Mol Cell, 2020. **80**(5): p. 810-827 e7.

1215 78. Gan, X., et al., *Inhibition of ERK-DLP1 signaling and mitochondrial division alleviates*
1216 *mitochondrial dysfunction in Alzheimer's disease cybrid cell.* Biochim Biophys Acta, 2014.
1217 **1842**(2): p. 220-31.
1218 79. Yu, T., B.S. Jhun, and Y. Yoon, *High-glucose stimulation increases reactive oxygen species*
1219 *production through the calcium and mitogen-activated protein kinase-mediated*
1220 *activation of mitochondrial fission.* Antioxid Redox Signal, 2011. **14**(3): p. 425-37.
1221 80. Han, X.J., et al., *CaM kinase I alpha-induced phosphorylation of Drp1 regulates*
1222 *mitochondrial morphology.* J Cell Biol, 2008. **182**(3): p. 573-85.
1223 81. Yang, D., et al., *CaMK II -induced Drp1 phosphorylation contributes to blue light-induced*
1224 *AIF-mediated necroptosis in retinal R28 cells.* Biochem Biophys Res Commun, 2021. **559**:
1225 p. 113-120.
1226 82. Simula, L., M. Campanella, and S. Campello, *Targeting Drp1 and mitochondrial fission for*
1227 *therapeutic immune modulation.* Pharmacol Res, 2019. **146**: p. 104317.
1228 83. Tortosa, E., et al., *Stress-induced vesicular assemblies of dual leucine zipper kinase are*
1229 *signaling hubs involved in kinase activation and neurodegeneration.* EMBO J, 2022.
1230 **41**(14): p. e110155.
1231 84. Otera, H., N. Ishihara, and K. Mihara, *New insights into the function and regulation of*
1232 *mitochondrial fission.* Biochim Biophys Acta, 2013. **1833**(5): p. 1256-68.
1233